Imaging affective and non-affective touch processing in two-year-old children

Maria, Ambika

2022-05-01

Maria , A , Hirvi , P , Kotilahti , K , Heiskala , J , Tuulari , J J , Karlsson , L , Karlsson , H & Nissilä , I 2022 , ' Imaging affective and non-affective touch processing in two-year-old children ' , NeuroImage , vol. 251 , 118983 . https://doi.org/10.1016/j.neuroimage.2022.118983

http://hdl.handle.net/10138/342634
https://doi.org/10.1016/j.neuroimage.2022.118983

NeuroImage 251 (2022) 118983

Contents lists available at ScienceDirect

NeuroImage

journal homepage: www.elsevier.com/locate/neuroimage

Imaging affective and non-affective touch processing in two-year-old children

Ambika Maria[a,b], Pauliina Hirvi[c,d], Kalle Kotilahti[c,a], Juha Heiskala[e], Jetro J. Tuulari[a,b,h], Linnea Karlsson[a,b,f,g], Hasse Karlsson[a,b], Ilkka Nissilä[c,*]

[a] University of Turku, Department of Clinical Medicine, Turku Brain and Mind Center, FinnBrain Birth Cohort Study, Finland
[b] University of Turku and Turku University Hospital, Department of Psychiatry, Finland
[c] Aalto University, Department of Neuroscience and Biomedical Engineering, P.O. Box 12200, AALTO FI-00076, Finland
[d] Aalto University, Department of Mathematics and Systems Analysis, Finland
[e] HUS Medical Imaging Center, Clinical Neurophysiology; Clinical Neurosciences, Helsinki, University Hospital and University of Helsinki, Helsinki, Finland
[f] University of Turku and Turku University Hospital, Department of Paediatrics and Adolescent Medicine, Finland
[g] Centre for Population Health Research, Turku University Hospital and University of Turku, Turku, Finland
[h] Turku Collegium for Science, Medicine and Technology, TCSMT, University of Turku, Finland

ARTICLE INFO

Keywords:
Affective touch
Child
Development
Insula
Diffuse optical tomography
Optical properties

ABSTRACT

Touch is an important component of early parent-child interaction and plays a critical role in the socio-emotional development of children. However, there are limited studies on touch processing amongst children in the age range from one to three years. The present study used frequency-domain diffuse optical tomography (DOT) to investigate the processing of affective and non-affective touch over left frontotemporal brain areas contralateral to the stimulated forearm in two-year-old children. Affective touch was administered by a single stroke with a soft brush over the child's right dorsal forearm at 3 cm/s, while non-affective touch was provided by multiple brush strokes at 30 cm/s. We found that in the insula, the total haemoglobin (HbT) response to slow brushing was significantly greater than the response to fast brushing (slow > fast). Additionally, a region in the postcentral gyrus, Rolandic operculum and superior temporal gyrus exhibited greater response to fast brushing than slow brushing (fast > slow). These findings confirm that an adult-like pattern of haemodynamic responses to affective and non-affective touch can be recorded in two-year-old subjects using DOT. To improve the accuracy of modelling light transport in the two-year-old subjects, we used a published age-appropriate atlas and deformed it to match the exterior shape of each subject's head. We estimated the combined scalp and skull, and grey matter (GM) optical properties by fitting simulated data to calibrated and coupling error corrected phase and amplitude measurements. By utilizing a two-compartment cerebrospinal fluid (CSF) model, the accuracy of estimation of GM optical properties and the localization of activation in the insula was improved. The techniques presented in this paper can be used to study neural development of children at different ages and illustrate that the technology is well-tolerated by most two-year-old children and not excessively sensitive to subject movement. The study points the way towards exciting possibilities in functional imaging of deeper functional areas near sulci in small children.

1. Introduction

Touch is one of our first senses to develop (Gottlieb et al., 1971) and plays a crucial role in our development and emotional well-being (Gallace and Spence, 2010). Gentle touch and caressing form a very important component of early parent-child interaction, especially in social bonding and secure attachment during the early years (Harlow, 1958; Dunbar, 2010; McGlone et al., 2014; Davidovic et al., 2016). Maternal affectionate touch is akin to the licking and grooming behaviour seen in most mammals (Feldman et al., 2010), and animal studies have indicated that it helps infants' stress regulation (Champagne, 2008; Hofer, 1995; Meaney, 2001). Correspondingly, according to studies in humans, maternal affectionate touch attenuates infants' physiological reactivity to stress and contributes to their neurobehavioral, cogni-

Abbreviations: DOT, diffuse optical tomography; CT, C-tactile; FD, frequency-domain; TD, time-domain; CW, continuous-wave; SDS, source–detector separation; TTL, transistor-transistor logic; SRE, surface registration error; PMT, photomultiplier tube; AAL, automated anatomical labelling; SS, scalp and skull; CSF, cerebrospinal fluid; GM, grey matter; WM, white matter; MWF, myelin-to-water fraction.

* Corresponding author.
E-mail address: ilkka.nissila@aalto.fi (I. Nissilä).

https://doi.org/10.1016/j.neuroimage.2022.118983.
Received 7 June 2021; Received in revised form 22 December 2021; Accepted 7 February 2022
Available online 9 February 2022.

tive, and social-emotional growth (Feldman and Eidelman, 2003, 2004; Feldman et al., 2010). Also, paternal skin-to-skin contact has been associated with improved bio-physiological markers in infants, such as respiration, oxygenation, glucose levels, and cortisol (Bauer et al., 1996; Christensson, 1996; Mörelius et al., 2015; Shorey et al., 2016), as well as better behavioural responses, such as less crying, better vocal interactions, and being relaxed (Erlandsson et al., 2007; Shorey et al., 2016; Velandia et al., 2012).

Mechanoreceptive properties of touch are thought to be carried out principally by two pathways within the peripheral nervous system: rapidly conducting, large, myelinated Aβ afferent fibres (afferents) relay non-affective or discriminative touch, while slowly-conducting, thin, unmyelinated C-tactile (CT) afferent fibres relay affective or emotional touch (Bessou et al., 1971; Björnsdotter et al., 2010; McGlone et al., 2014; Morrison, 2016; Olausson et al., 2010). CT afferents have been found on the face (Nordin, 1990) and in hairy skin such as in the forearm, in humans (Löken et al., 2009; McGlone et al., 2014; Vallbo et al., 1993, 1999). CT afferents have been reported to respond maximally to slow stroking at the speed of 1–10 cm/s which has been rated by adult human subjects as the most pleasant (Löken et al., 2009; Ackerley et al., 2014a). In contrast, brushing at a speed of 30 cm/s mainly activates myelinated afferents and is not perceived as pleasant (Löken et al., 2009). Affective touch has been reported to cause heart rate deceleration which is indicative of decreased arousal, increased behavioural engagement and interest in the stroking brush, in nine-month-old infants (Fairhurst et al., 2014). Pawling et al. reported significantly greater activation of the zygomaticus major (smiling muscle) in response to CT-optimal stroking (3 cm/s) on the forearm than the palm or CT-non-optimal stroking (30 cm/s) to the forearm or palm. These results provided the first empirical behavioural evidence in humans that CT-optimal touch carries a positive affective valence that can be measured implicitly (Pawling et al., 2017). Furthermore, touch on the hairy skin of the forearm has been seen to have a greater affective value than touch on the glabrous skin of the palm (Olausson et al., 2010; McGlone et al., 2012; Ackerley et al., 2014b; Pawling et al., 2017).

Olausson et al. used functional magnetic resonance imaging (fMRI) to study two patients who had intact CT afferent pathways but lacked functioning Aβ afferent pathways and discovered activation in the insula and deactivation in the primary somatosensory cortex (S1) in response to CT-optimal touch in these subjects (Olausson et al., 2002; Olausson et al., 2008). In healthy subjects, several additional brain areas are involved in processing of CT-optimal touch: the secondary somatosensory cortex (S2), superior temporal sulcus (STS), middle temporal gyrus (MTG), insular operculum, temporoparietal junction, medial prefrontal cortex, anterior cingulate cortex (ACC), amygdala, inferior frontal gyrus (IFG), and orbitofrontal cortex (Olausson et al., 2002; Lindgren et al., 2012; Gordon et al., 2013; Voos et al., 2013; Björnsdotter et al., 2014; Bennett et al., 2014; Kaiser et al., 2016; Sailer et al., 2016; Jönsson et al., 2018; Pirazzoli et al., 2019; Tuulari et al., 2019).

Given the importance of affective touch in forming social bonds, affective touch processing has been increasingly studied in infants and adults. Brain responses to affective touch have been observed in infants as early as 11–36 days after birth (Tuulari et al., 2019). Björnsdotter et al. studied affective touch responses in adult-defined regions of interest (S1, S2, insula and posterior STS) using fMRI in healthy 5–13-year-old children, adolescents (14–17 years of age) and adults (25–35 years of age), finding similar activation in all age groups (Björnsdotter et al., 2014). In this study, we aim to bridge the gap in studies of affective touch processing between infants and 5-year-olds by imaging children at the challenging age of two years.

Near-infrared spectroscopy (NIRS) is well-suited for imaging infants and children (e.g., Lloyd-Fox et al., 2010; Maria et al., 2020) as it is regarded less sensitive to movement than fMRI or electroencephalography (EEG) and allows imaging in a more naturalistic environment where the child can interact socially and be in the presence of a parent or sibling (Maria et al., 2018). Diffuse optical tomography (DOT) is based on the physical principle of NIRS extended into 3D imaging with several partially overlapping measurements and model-based image reconstruction (Arridge, 1999; Gibson et al., 2006; Zeff et al., 2007; Heiskala et al., 2009a; Liao et al., 2012; Jönsson et al., 2018). DOT is primarily a functional imaging modality where the most prominent physiological contrast arises from the absorption of light by oxygenated and deoxygenated haemoglobin. However, the light transport and reconstructed images are sensitive to the optical properties of the underlying tissue, and greater accuracy can be obtained if the shape, structure and optical properties of the underlying tissue are known (Heiskala et al., 2009a; Heiskala et al., 2009b) or can be estimated from the data. DOT instruments can be divided into three categories: continuous-wave (CW) systems typically use millisecond pulses and/or intermediate frequency (~ kHz) modulated light source and record the intensity of the detected light or the modulation amplitude (Zeff et al., 2007). Time-domain (TD) systems use picosecond pulses of light and record the time-of-flight distribution of the detected photons (Schmidt, 2000). Frequency-domain (FD) systems use radiofrequency intensity-modulated light and measure the phase shift and amplitude of the detected photon density wave (Boas, 1996; Chance, 1998). TD and FD data types can be used to distinguish between the effects of scattering and absorption and estimate the baseline optical properties of the tissue in conjunction with prior information. CW devices are the most common due to their lower cost and complexity, compactness, and greater signal-to-noise ratio (SNR) at short to medium source–detector separations (SDSs). However, at longer SDSs, photomultiplier tube (PMT) detectors commonly used in TD and FD systems have the SNR advantage (Nissilä 2004; Nissilä et al., 2005b). As we seek to image regions deeper than the outer surface of the cortex, the accurate modelling of light transport in the tissue and SNR at long SDSs become increasingly important.

Previous studies on touch with fNIRS or DOT in children have targeted infants; Gibson et al. (2006) studied passive motor responses in very preterm infants using whole-head time-resolved 3D DOT. In Jönsson et al. (2018), we studied the affective and non-affective touch processing in two-month-old infants using DOT and found the statistically most differentiating area between affective and non-affective touch within the field of view of the study to be in the insula. Pirazzoli et al. did not find significant differences in responses to affective and non-affective touch in 5-month-old infants with fNIRS (Pirazzoli et al., 2019).

In the present study, we used intensity-modulated (FD) DOT (Nissilä et al., 2005a) with a high-density probe to study affective and non-affective touch processing in the left frontotemporal brain areas of two-year-old children. High-density optode arrangements with many partially overlapping measurements improve image quality and reduce inter-subject variability arising in sparse arrangements from slight variations in the positioning of individual optodes relative to the location of activity (Zeff et al., 2007; Heiskala et al., 2009a). The left hemisphere (LHS) was chosen for imaging since the brain–scalp distances reported by Beauchamp et al. (2011) in 18-month to 5-year-old children are shorter, on average, in the LHS than the right hemisphere (RHS) which is expected to lead to a slightly higher measurement sensitivity and increased contrast for cortical hemodynamic changes in the LHS. Regions within the field-of-view (FOV) include the areas which are most likely activated by affective and discriminative touch in fMRI studies, including the insula, S1, and S2 contralateral to the stimulated forearm (Morrison, 2016; Perini et al., 2015; Olausson et al., 2002; Gordon et al., 2013). Since subject-specific anatomical MR images were not available, we used a published age-appropriate atlas template (Shi et al., 2011) and deformed it to match the shape of each subject's head based on photogrammetry. Given the lack of published data on optical properties in two-year-olds, we elected to use literature (adult) optical property values for the cerebrospinal fluid (CSF) and white matter (WM) and obtained estimates for the optical properties of the combined scalp and skull compartment and the grey matter (GM) by fitting the forward model predictions to match measured and calibrated phase and log am-

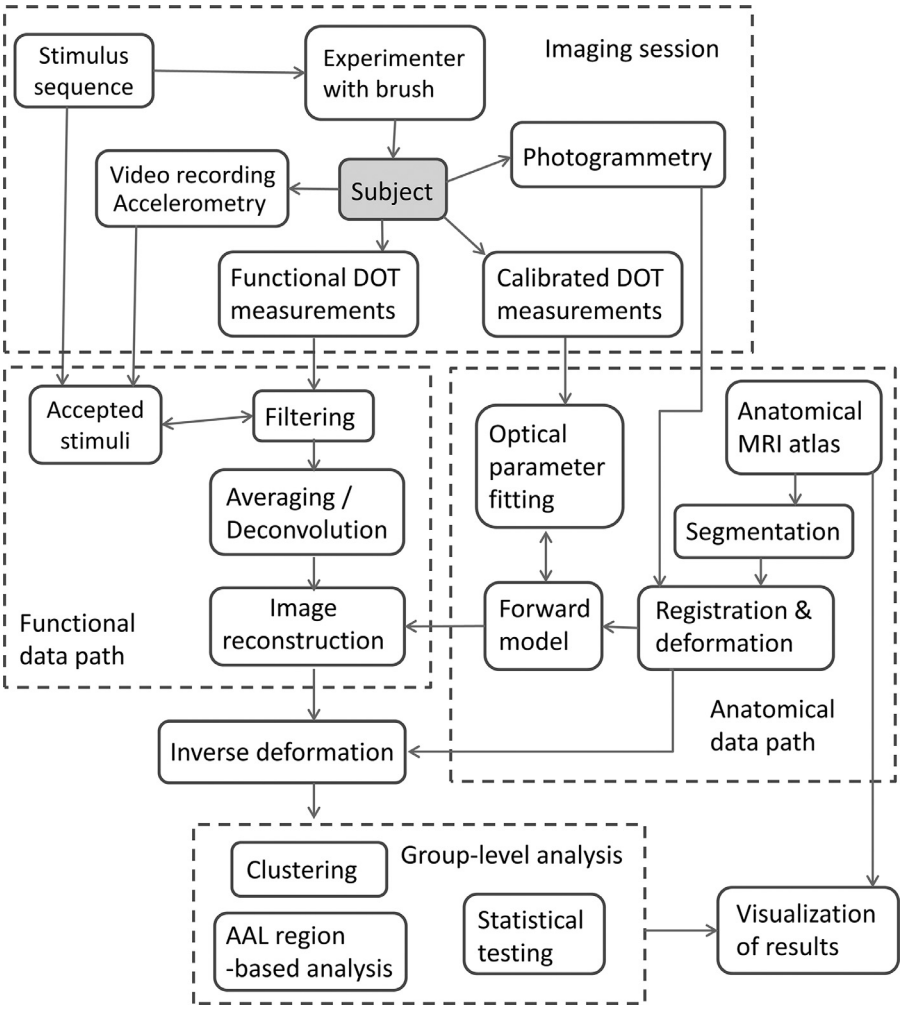

Fig. 1. Overview of the data flow from the measurement session via the anatomical and functional pipelines to the group-level statistical analysis and visualization of the results. AAL = automated anatomical labelling.

plitude data in a least-squares sense. This allowed us to fine-tune our model to the subject population, achieving more accurate modelling of light transport in the tissue and improving the accuracy of the functional imaging as well.

For two-year olds, our main hypotheses are that the insula as the primary cortical target of CT afferent fibres is activated to affective touch more than non-affective touch, whereas the primary somatosensory cortex is likely to be activated to a greater degree to non-affective touch than affective touch due to our implementation of non-affective touch consisting of multiple fast brush strokes.

2. Materials and methods

The study was approved by the Ethics Committee of the Hospital District of Southwest Finland and was conducted in accordance with the Declaration of Helsinki (decision ETMK 31/180/2011 § 534 Nov 17, 2015). An overview of the measurements and data analysis is given as a flow chart in Fig. 1 and a detailed description of the pipeline is given below.

2.1. Study participants

25 two-year-old children (12 girls and 13 boys) from the FinnBrain Birth Cohort Study (Karlsson et al., 2018) participated in this experiment. Families in which children were born between January and April 2014 were randomly selected and recruited through a personal phone call by a research nurse. Additional inclusion criteria were children born full-term (36–42 weeks of gestation) with the mother having no history of neurological, medical or psychiatric disorders. The participant families were given oral and written information about the study prior to the measurements. The parents gave written informed consent on behalf of their child. All the families were Finnish. The mothers were non-smoking and the maternal prenatal monthly income averaged between 2000 and 2500 euros, which could be considered as middle-class income in Finland (Statistics Finland, 2017). Out of the 25 measurements, 9 measurements were unsuccessful either because the parent or one of the experimenters stopped the experiment if the child got restless ($N = 2$), there was extensive jaw movement ($N = 1$) or we got insufficient data for analysis for technical reasons ($N = 6$). Thus, the final sample consisted of 16 children (8 girls and 8 boys). Table 1 shows descriptive statistics of the children included in this study.

2.2. Measurement session

The measurements were carried out in a room with dimmed ambient lighting in the afternoon (noon to 6 p.m.). This time range was provided as convenient for the families so that they could incorporate the measurements into family routines such as nap times and eating. Prior to the neuroimaging session, the child and parent were given some time to familiarize themselves with the scanning environment. The child was encouraged to play for some time (typically about 10 min) until they were calm and comfortable with the surroundings and the experimenters.

During the session, the parent was asked to sit on a comfortable chair holding the child on their lap (Fig. 2a) and not to talk to the child unnecessarily. The child was presented videos of a pre-selected neutral

Table 1
Descriptive Statistics of Children in the study (N = 16).

Characteristic	Median	Range
Age at measurement calculated from term (days / years)	756 / 2.1	708–800 / 1.9–2.2
Age at measurement calculated from the birthdate (days / years)	752 / 2.1	734–786 / 2.1–2.2
Gestational weeks at birth	40	36–42
Head circumference of the child at birth (cm)	36	33–38
Birth weight (g)	3663	2885–4900
Birth height (cm)	52	47–56
Maternal age at measurement (years)	36	24–47
Maternal age at birth (years)	34	21–45
Maternal Pre-pregnancy Body Mass Index (BMI)	24	19–36

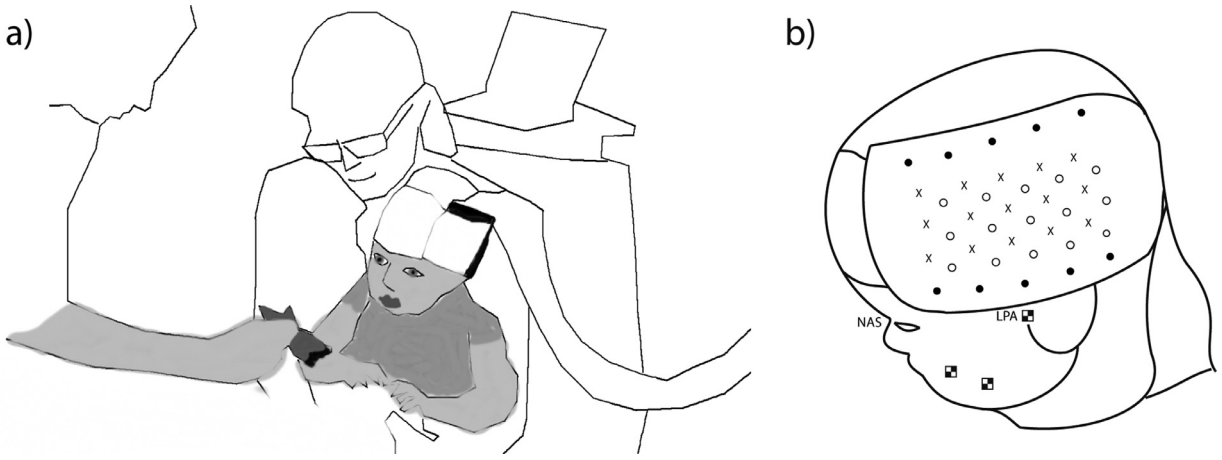

Fig. 2. Experimental session. a) Illustration of the measurement setup with the experimenter providing the brushing stimuli with a soft paintbrush to the child's right forearm. b) Placement of the measurement probe over the left frontotemporal cortex of the child. NAS = nasion, LPA = left preauricular point, 'X' = source, circle = detector, black filled circle = extra photogrammetry marker.

cartoon to help motivate the child to sit still for the entire course of the measurement session. We adopted this paradigm since in previous studies with touch experiments on infants, silent videos were found to capture the infant's attention and improve the signal-to-noise ratio of measured data (Fairhurst et al., 2014; Miguel et al., 2019). Photogrammetry markers were placed on the child's head while they were sitting on their parent's lap. A stereo camera setup was used to record images of the child and the markers from different directions.

A silicone-based (Accutrans Black, Ultronics/Coltène) high-density fibre-optic probe with 15 source fibres and 15 detector fibre bundles, each equipped with a 4-mm right-angle prism terminal, was placed over the left frontotemporal cortex of the child (Fig. 2b). It was held in place by a self-adhesive bandage wrapped around the child's head. After the probe was attached, additional stereo images were taken to record the position of the probe relative to landmarks. The course of the whole measurement session was recorded using a video camera. If the child was uncomfortable or crying, the measurement was paused for consoling the child before continuing. Once the child was calm again, the parent was asked for the permission to continue.

2.3. Stimuli

A trained experimenter (author AM) manually stroked the child's right dorsal forearm skin using a soft goat-hair paintbrush. A laptop computer running Presentation© software (Neurobehavioral Systems) showed "Slow" and "Fast" cues after a countdown for nine seconds prior to the onset of the next stimulus to cue the experimenter to be ready at the correct time. The stimulus onset trigger was transmitted using a parallel port signal between the stimulus laptop and the DOT instrument control and data acquisition computer. An optoisolator was used to make sure the trigger signal did not cause electrical interference. The trigger signal consisted of transistor-transistor logic (TTL) pulses with length indicating the stimulus condition; 50 ms = slow brushing and 100 ms = fast brushing.

Slow brushing was carried out with a single stroke in a proximal-to-distal direction at an approximate speed of 3 cm/s (affective touch) while fast brushing was administered with 7–9 strokes in alternating direction at an approximate speed of 30 cm/s (non-affective touch). Similar stroking velocities have been used in prior neuroimaging studies on affective touch processing (Olausson et al., 2002; Jönsson et al., 2018; Tuulari et al., 2019). The stimuli were presented in an event-related fashion where the stimulus was applied for 2 s, with an average inter-stimulus interval of 31 s (range 12 to 127 s, standard deviation 20 s). An average of 59 stimuli (30 slow and 29 fast) were presented per child in a randomized counterbalanced order. The length of the brushing stroke was approximately 6 cm over the right forearm for both the slow and fast stroking, and the speed of brushing was confirmed from the video recordings. A stimulus robot was not used because it would have required fixing the position of the arm, which was not feasible given the age of the subjects.

We aimed to acquire data for 2 measurement runs, comprising 80 stimuli per child, although for one child, three runs were acquired (120 stimuli). The total duration of one measurement run was approximately 25 min. The duration of one complete measurement session was approximately 1–1.5 h (including 10 min for familiarization). The entire measurement session was video-recorded in order to detect and discard motion artefacts and make note of missed stimuli in subsequent analysis.

2.4. Instrumentation

A 16-channel frequency-domain (FD) diffuse optical tomography (DOT) system was used for this experiment (Nissilä et al., 2002, 2005a). The light is intensity modulated at 100 MHz and the source fibres are illuminated in a time-multiplexed sequence. The system records both am-

plitude and phase data which closely correspond to intensity and mean time of flight in time-domain systems. The gains of the photomultiplier tube (PMT) detectors are adjusted during the imaging sequence to optimize the signal-to-noise ratio for each source–detector pair. A microelectromechanical system (MEMS) technology switch (Opneti Ltd., China) was used to switch between the source fibres, with 50 ms pulse duration and 20 ms high voltage adjustment settling time between source positions, leading to a total image acquisition time of 1.4 s. An accelerometer was embedded in the silicone probe to provide information on the child's movements.

A single 798 nm wavelength was used, allowing us to optimize the time resolution and SNR. The laser diode temperature was regulated to maintain the target wavelength which was confirmed using a spectrometer before and after the measurement series. This wavelength allows the determination of changes in the total haemoglobin concentration (HbT). Synaptic activity modulates arteriolar dilation and contraction through the neurovascular coupling and the resulting changes in vascular diameter contribute to changes in HbT (Hillman et al., 2007; Devor et al., 2007). Hillman et al. studied HbO_2, HbR and HbT responses to forepaw stimulation in the rat and found that the arteriolar and capillary compartments contributed more to the HbT time course than the HbO_2 and HbR time courses and the venous compartment had the smallest contribution in the HbT signal (Hillman et al., 2007). Culver et al. observed that HbO_2 and HbR include significant contributions from venous drain areas whereas the HbT response was more localized to the arteriolar side, leading to greater spatial accuracy and resolution when the intention is to localize sites of neuronal activity (Culver et al., 2005). Gagnon et al. showed that the cortical contribution to the HbT signal in the motor cortex is greater and the pial vein contribution to the HbT signal smaller than in HbO_2 and HbR signals (Gagnon et al., 2012). In a review of NIRS studies on infants by Lloyd-Fox et al. (2010), most studies included show statistically significant positive HbO_2 responses to stimuli whereas the polarity of HbR responses varies from study to study and subject to subject. A few studies show inverted polarity in both HbO_2 and HbR. Statistics on HbT are only reported in a minority of studies, but the polarity of HbT generally aligns with HbO_2.

2.5. Raw signal processing

The measured amplitude data was used to estimate the haemodynamic response time course for each source–detector pair and stimulus condition. The data for each source–detector pair was resampled to a common time base with 2 Hz sampling frequency using linear interpolation. Signal drift was removed by subtracting a piecewise linear function fit to averaged signal values within [−2 s, 0 s] pre-stimulus intervals that precede blocks of stimuli with inter-stimulus-interval (ISI) ≤ 20 s from the original signal. The video recordings of the session were analysed to determine epochs with head movements, limb movements, or crying. Motion artefacts were additionally detected using the following two criteria: a) epochs where the accelerometer signal exceeded a fixed threshold or b) where the difference between the minimum and maximum of the filtered optical amplitude signal exceeded seven times the standard deviation of the signal. Artefactual epochs were excluded from further analysis. Finally, the raw signals were low-pass filtered at a cutoff frequency of $f_{-3\,dB} = 0.2$ Hz.

In this study, because we were concerned with the impact of the child's activity during resting periods on the resulting haemodynamic response time courses, instead of averaging with finite impulse response deconvolution, we used a predefined haemodynamic response function (HRF) kernel and determined the response magnitude by minimizing the squared error between the model-predicted and measured raw data. The measured log amplitude signal y can be considered as a linear convolution of a filter kernel h and the stimulus onset vector s_i, where i = the stimulus condition type (1 = slow brushing, 2 = fast brushing). The convolution can be expressed in matrix format with

$$S_i = s_i \otimes h,$$

$$y = Sb + n,$$

$$S = \begin{bmatrix} S_1 & S_2 & 1 \end{bmatrix},$$

$$b = \begin{bmatrix} b_1 \\ b_2 \\ b_3 \end{bmatrix},$$

where n is a noise vector which includes physiological signals unrelated to the neuronal activity as well as measurement noise, and b is a column vector where b_1 is the magnitude of the response corresponding to slow brushing, b_2 for fast brushing and b_3 a constant which sets the baseline level. The haemodynamic response function kernel h is the canonical HRF model from the SPM software (analytical formula given in Lindquist et al., 2009) with default parameters convolved with a two-second boxcar function and time scaled by 1.25x to achieve a realistic time-to-peak of 7 s that was consistent with the responses in the raw data (Fig. 3b).

Vector b can then be estimated by solving the set of linear equations using MATLAB's `mldivide` operation,

$$\hat{b} = S \backslash y.$$

The final data comprised 16 children (8 boys and 8 girls) from whom we had artefact-free signal for responses to at least 10 stimuli. The average numbers of stimuli presented for the included children were 37 and 36 for slow and fast brushing, respectively, and on average, 27 slow and 28 fast stimuli were accepted into averaging. The total numbers of stimuli accepted into averaging for all included subjects were 438 for slow and 445 for fast brushing.

Prior to the actual experiment with stimuli, a measurement with a slower sequence (500 ms pulse for each source position) was made to record information on the baseline optical properties of the tissue. The measured phase and amplitude data were calibrated to correct for differences in transmission, sensitivity, and time-of-flight between individual source and detector channels, and for the effect of high-voltage gain adjustment on the amplitude and phase. The detector gain calibration procedure is described in (Nissilä et al., 2002, 2005a) and the procedure for compensating for interchannel differences in the attenuation and optical pathlength was adapted from Hillman et al. (2000).

2.6. Photogrammetry

Before starting the measurement, a stretchable coloured glass pearl marker mesh (with an average of 60 photographed pearls) was placed on the subject's head. In addition, marker stickers were positioned at the left and right preauricular points (LPA and RPA, respectively), the nasion (NAS), on the cheeks and the chin. Two Olympus E-PL5 cameras with Leica Panasonic 25 mm f/1.4 lenses were mounted in an aluminium frame and synchronized using an electrical remote release. A studio flash and reflector were used to bounce light from the room's white ceiling to produce even, diffuse lighting. Flash-based lighting was used to minimize blur due to subject movement and produce high quality images with consistent quality of light and colour across multiple different camera angles. The flash was triggered using a radio trigger. The internal and external calibration parameters of the stereo camera model were determined by taking synchronized exposures of a calibration target which consists of three orthogonal plates with a black square on a white background. DXO Optics Pro software was used to process the raw images and apply distortion correction.

Stereo images captured from 5 to 7 different angles of the head with the pearl mesh and from one angle with the probe attached on the head were used to identify matching points between the left and right cameras and estimate the corresponding 3D coordinates. Matching points between stereo image pairs were also marked, and rigid translation and rotation were used to combine the 3D point sets from each camera angle. The multiple reconstructions of a point from different camera angles were replaced with their average.

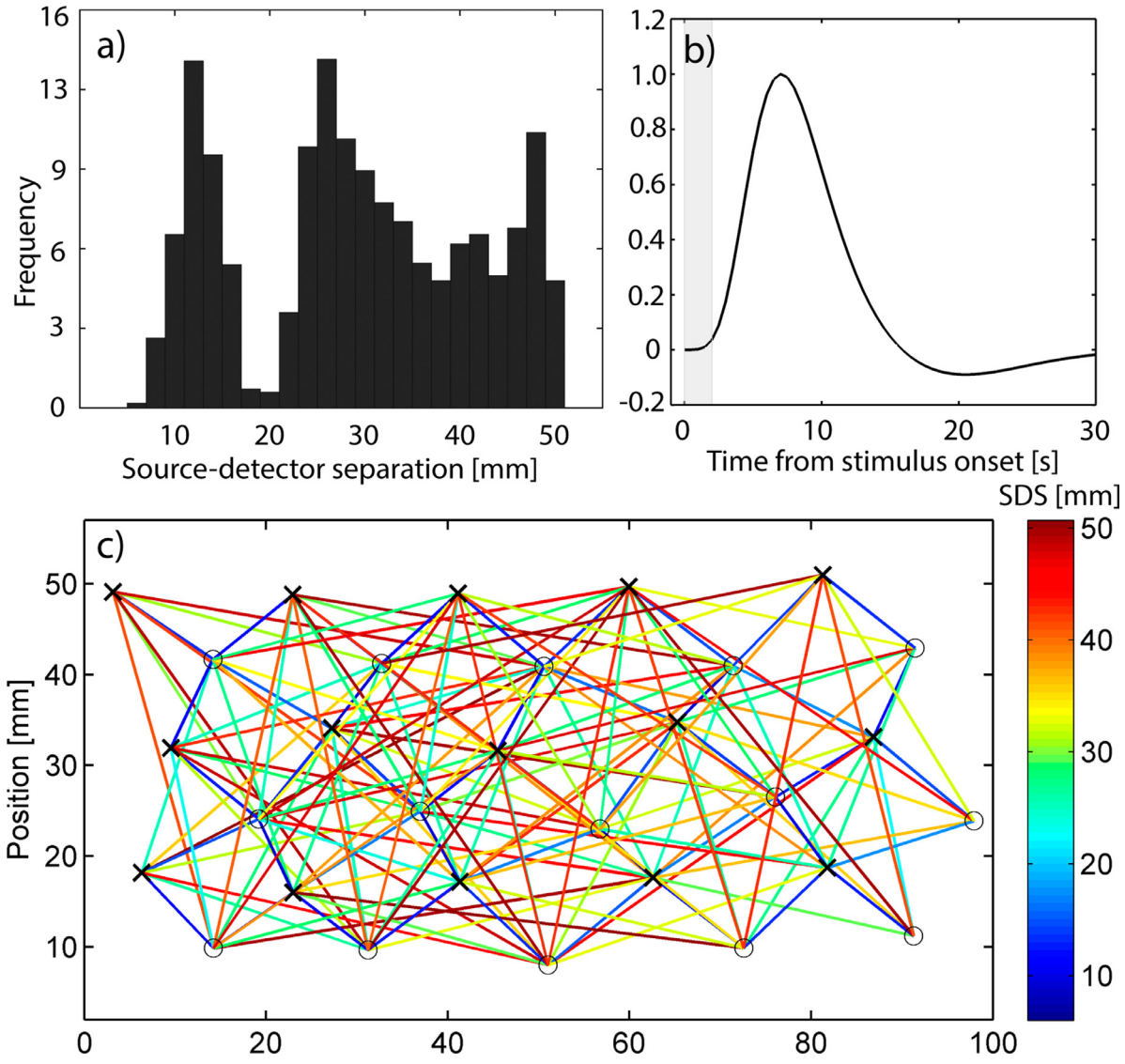

Fig. 3. Optode arrangement and shape of the haemodynamic response function (HRF). a) Histogram of source–detector separations (SDS) used in the study. b) Time course of the haemodynamic response function used in the analysis; vertical grey bar indicates stimulus timing. c) Approximate layout of the source and detector optodes in the grid. 'X' = source, 'O' = detector position. The colour coding indicates separation between source and detector. (Figure should be printed in colour.).

2.7. Anatomical head model and optode positions

The anatomical head models required for the forward and inverse modelling and visualization of results were obtained by registering a published age-appropriate template (Shi et al., 2011) to the individual head shapes measured with photogrammetry. Previously, atlas-guided DOT has been studied, for example, by Gibson et al., 2003; Heiskala et al. (2007b, 2009b) Custo et al. (2010), and Ferradal et al. (2014). The size of the template is 181 × 217 × 181 and it consists of isotropic cubic voxels with a side length of 1 mm. The template included tissue type probability maps for cerebrospinal fluid (CSF), grey matter (GM) and white matter (WM), and an averaged intensity image. The probabilities were converted into a fixed model by first defining the GM and WM to consist of the voxels where the probability of the respective tissue type was the highest. The combined scalp and skull layer was created by thresholding the template intensity image and excluding the previously assigned voxels. The brain–scalp distances in the model were compared with those published in Beauchamp et al. (2011) and found to be a reasonably good match. The CSF segmentation was refined manually to separate the subarachnoid CSF with arachnoid trabeculae from the sulcus and ventricular CSF, and to obtain a realistic subarachnoid CSF thickness and total volume of CSF. The maximum absolute difference between a tissue's volume ratio in the atlas versus in the deformed template is under 0.1 percentage points for all subjects.

The landmarks (LPA, RPA and NAS) were used to transform the 3D points from photogrammetry into the template's coordinate system. The marker mesh is sparse enough that it was generally not significantly lifted by hair. In the case of braids, the affected points were removed. The points marked with a pearl were dropped radially towards the estimated centre of the head to account for the pearl height. The Iso2Mesh toolbox (Fang and Boas, 2009a) was used to generate a triangular surface mesh for the template, with a maximum Delaunay sphere radius of 5 mm resulting in a mesh with 4868 triangles (2393 nodes). The optimal deformation for the template was searched as the one that best matches the mesh surface to the target surface points.

A nine-parameter affine transformation, including anisotropic scaling, rotation and translation was chosen for the registration, as described in (Hirvi, 2019). This enabled controlled modification of the template shape, in addition to rigid deformations as in (Wu et al., 2014, 2015). To find the optimal deformation, the iterative parameter grid search algo-

Table 2
Optical properties used in the tissue model. μ_s' = reduced scattering coefficient, μ_a = absorption coefficient, g = anisotropy factor, n = index of refraction.

	μ_s' [mm^{-1}]	μ_a [mm^{-1}]	g	n
Scalp & Skull	0.8	0.012	0.9	1.35
CSF-1	0.3	0.004	0.9	1.35
CSF-2	0.001	0.002	0.9	1.35
Grey Matter	2.2	0.014	0.9	1.35
White Matter	8.4	0.0032	0.9	1.35

rithm from Mäkelä et al. (2001) and (Koikkalainen and Lötjönen, 2004) was implemented. The main term in the objective function was the surface registration error (SRE) calculated as the average distance from the target points to their closest points on the mesh (surface-based registration) (Frisch, 2018; Koikkalainen and Lötjönen, 2004). The closest points were re-calculated for each deformation, and the target set included the pearl-marked points and the preauricular landmarks. For two of the subjects, the nasion was also included in the SRE, but for the rest, more accurate and realistic results were obtained by including constraint terms in the objective function that set the upper limits to the point-wise Euclidean separation between the template and target nasion. Following the template deformations, the average SRE for the pearl-marked surface points over all subjects decreased from 8.0 ± 3.4 mm to 1.6 ± 0.3 mm (for denser surface meshes with maximum Delaunay radius of 2 mm). The templates were deformed using MATLAB's imwarp function and cubic interpolation to define new tissue boundaries. The optode positions on the scalp were interpolated using the visible markers on the probe, the known geometry of the probe and the surface of the deformed anatomical model. We validated the processes via careful visual evaluation of the deformed models and the optode positions.

2.8. Optical properties in the tissue model

The tissue-specific optical properties in the five-compartment model of the optical structure of the head are presented in Table 2. The anisotropy factor was set to $g = 0.9$ and index of refraction to $n = 1.35$ for all tissue types. The CSF was divided into the subarachnoid CSF (CSF-1) containing the subarachnoid trabeculae, and the low-scattering CSF (CSF-2) consisting of the CSF in the sulci and ventricles. The optical properties we selected for the CSF are in agreement with (Okada and Delpy, 2003), whose simulations suggest that the effect of arachnoid trabeculae could be modelled with a homogeneous semidiffusive tissue type with reduced scattering of 0.16–0.32 mm^{-1}, and CSF without the trabeculae is given absorption of 0.002 mm^{-1} and reduced scattering of 0.001 mm^{-1}, as also in Heiskala et al. (2007a) for ventricular CSF. The properties for WM were estimated from the graphs and the reported values by van der Zee et al. for *post mortem* measurements in adults at the wavelength of 800 nm (van der Zee, 1993a; Van der Zee et al., 1993b). The WM absorption and scattering coefficients reported by van der Zee et al. were measured from 50-, and 60-year-old subjects. Deoni et al. estimated myelin-to-water-fraction (MWF) in children between approximately 3 months and 5 years of age using MRI (Deoni et al., 2016). We estimated MWF values visually from the graphs at two years of age as 0.11–0.13 for temporal, parietal and frontal areas. Faizy et al. estimated the MWF of frontal and parietal WM for 50–60-year-old adults to be approximately 0.9–0.12 (Faizy et al., 2018). Based on these considerations and in the absence of direct data, we assume the MWF and WM optical properties for two-year-olds to be closer to those of adult subjects rather than neonates.

We estimated the optical properties for combined scalp and skull layer (SS), and GM by simulating the logarithm of amplitude $\ln(A)$ and phase shift φ data for different optical parameter combinations to find the data that best fits the measurements after accounting for coupling variations in the amplitude measurements and baseline drift in the calibrated phase. For each source–detector pair, we used the Monte Carlo eXtreme software (see Sec. 2.9) to obtain the partial pathlengths $l_{p,m}$ for each medium m that are converted to total time of flights t_p for each detected photon packet p. The logarithm of amplitude and phase shift are computed using the following formulas (Heiskala 2009c):

$$X = \sum_p \exp\left(-\sum_m \mu_{a,m} l_{p,m}\right)\cos\left(2\pi f t_p\right),$$

$$Y = \sum_p \exp\left(-\sum_m \mu_{a,m} l_{p,m}\right)\sin\left(2\pi f t_p\right),$$

$$\ln(A) = \ln\left(\sqrt{\left(X^2 + Y^2\right)}\right),$$

$$\varphi = \arctan\left(\frac{Y}{X}\right),$$

where f is the modulation frequency of 100 MHz and $\mu_{a,m}$ is the absorption coefficient for tissue type m.

The baseline for the simulated $\ln(A)$ values is set by matching the mean value over the SDS range 15–55 mm to the corresponding measured mean value. In this range, the simulated values exhibit a roughly linearly decreasing trend with respect to increasing SDS. For two of the 16 subjects, the absolute calibration was not performed and the phase baseline was fixed by fitting a line to the approximately linear part of the data and moving the data so that this line crosses the origin.

We simulated data in a four-dimensional grid of possible values for the four unknown optical parameters to cover a wide range of literature (Firbank et al., 1993; van der Zee, 1993a; Van der Zee et al., 1993b; Okada et al., 1997; Simpson et al., 1998; Bevilacqua et al., 1999; Schmidt, 2000; Torricelli et al., 2001; Yaroslavsky et al., 2002; Strangman et al., 2003; Fukui et al., 2003; Zhao et al., 2005; Custo et al., 2006; Gagnon et al., 2012; Dehaes et al., 2011; Hallacoglu et al., 2013; Farina et al., 2015; Farzam et al., 2017; Brigadoi and Cooper, 2015). The tested values for the absorption coefficient cover the range 0.005–0.06 mm^{-1} in steps of 0.005 mm^{-1} and include some intermediate literature-based values from the range 0.006–0.03 mm^{-1} for a total of 21 and 22 values for SS and GM, respectively. The tested scattering coefficient values cover the range 4–20 mm^{-1} and 4–28 mm^{-1} in steps of 2 mm^{-1}, for SS and GM, respectively. As a result, we have 117 different scattering coefficient combinations and a total of 54,054 different optical parameter combinations. The simulations take 2–3 h per scattering combination, for one subject and all source–detector pairs (225 in total).

For each set of optical parameters, we used MATLAB's `lsqlin` operation to find the column vector C of 31 coupling coefficients that minimize, in the least-squares sense, the difference between measurements and simulations, given as

$$W \cdot \left(y_{\text{meas}} + B \cdot C - y_{\text{simu}}\right),$$

where y_{meas} and y_{simu} are 481 × 1 column vectors with all $\ln(A)$ and phase values (maximum 225 for each), and 31 zeros at the bottom for the coupling coefficient regularization terms. Matrix B is a 481 × 31 binary selection matrix, and matrix W is a 481 × 481 diagonal weight matrix. In vector C, the 30 first elements are the actual coupling coefficients accounting mainly for the effects of hair on the $\ln(A)$ measurements. These coefficients are limited to non-negative values since hair has been observed to cause mainly drops in the amplitude values (Fig. 12 in Schweiger et al., 2007). The last unlimited element in C accounts for the baseline-drift in the calibrated phase measurements.

We computed W as the square root of the inverted covariance matrix assuming that the measurements are independent. Thus, each weight is obtained as the inverse of the variable's estimated standard deviation (STD). The STD of the phase measurements and the phase baseline was set as 1°, with the exception that the baseline is not regularized for the

two subjects without absolute calibration. The STD for $\ln(A)$ was obtained from this by scaling with the ratio of their mean values in the SDS range 15–55 mm. The STDs for the corresponding coupling coefficients are further scaled to account for the smaller number of coefficients compared to measurements.

Following the least-squares optimization with the coupling coefficients, the tested optical parameter combinations are arranged in order according to increasing squared error for each subject. The overall best set of properties is selected as the one with the lowest sum of rankings over all 16 subjects (Table 2).

2.9. Monte Carlo simulation

We use the Monte Carlo eXtreme (MCX/MCXLAB, v2020 "Furious Fermion"; Fang and Boas, 2009b; Yu et al., 2018) software to record the photon trajectories for computing the simulated FD data and the Jacobians or the sensitivities of the detected intensities to voxel-wise changes in the absorption coefficient for each source–detector pair. The sensitivities were estimated as the sum of the detected photon weights multiplied by the voxel-wise partial path lengths (Heiskala, 2009c) using the "replay" method in MCX (Yao et al., 2018).

We run the GPU-accelerated version of MCX on NVIDIA Tesla P100 and V100 GPU-cards provided by the Aalto Science-IT project. The cluster offers multiple GPU cards for use in parallel, which enables handling multiple subjects and optical parameter combinations simultaneously and accelerates the process. Each source was modelled as a collimated Gaussian beam with a waist radius of 1.25 mm. The detector radius was 1.82 mm. For each source, we simulated 10^9 photon packets for 90 ns. All simulations were performed in the 1 mm voxel grid, but the voxel size was increased to 2 mm for the image reconstructions. The obtained subject-specific Jacobians and reconstructions are inverse-deformed back to the atlas model to enable group-level analysis within the same reference template.

2.10. Image reconstruction

The voxel-wise absorption coefficient changes $\Delta\overrightarrow{\mu_a}$ were reconstructed from changes in the logarithm of amplitude obtained by fitting the HRF model to the measured amplitude signal (Section 2.5). The solution to the inverse problem was calculated with Tikhonov regularization (Heiskala et al., 2009a; Näsi et al., 2013) by minimizing

$$\sum_{s,d} \left(\Delta\ln\left[A_{\mathrm{MC}}\left(s,d,\Delta\overrightarrow{\mu_a}\right)\right] - \Delta\ln[A(s,d)]\right)^2 + \alpha\|\mathbf{L}\Delta\overrightarrow{\mu_a}\|_2^2,$$

where for each source (s) and detector (d), A is the measured amplitude and A_{MC} the estimated value according to the Monte Carlo simulations. The Laplacian matrix $\mathbf{L}$ is computed as

$$L_{ij} = \begin{cases} nn, & \text{if } i = j \\ -1, & \text{if } j \text{ is a neighbor of } i, \\ 0, & \text{otherwise} \end{cases}$$

where nn is the number of voxels with a common face with voxel i (6-neighbourhood). The inverse problem was linearized using the calculated Jacobians, and the least-squares solution to the matrix equation was obtained with MATLAB's `lsqr` operation. The regularization parameter value $\alpha = 10$ and the maximum number of iterations (100) were chosen as found appropriate in reconstruction of simulated cortical activation as well as phantom data. From the reconstructed changes in the absorption coefficient, changes in total haemoglobin (HbT) were calculated using extinction coefficients from Cope (1991).

Only the data from source and detector pairs with Euclidean separation under 50 mm were utilized for the reconstructions from functional data to avoid risk of low SNR or light leakage. The histogram of the source–detector separations (SDS) in the optode arrangement is given in Fig. 3a. The spatial arrangement of sources ('X') and detectors ('O') in the measurement probe is shown in Fig. 3c with interconnecting lines indicating source–detector pairs in use. For the purpose of defining the field of view (FOV) of the probe in the atlas template, we considered the falloff of measurement sensitivity of the probe in the following way: The normalized Jacobian was first calculated by dividing the inverse warped Jacobian with its largest value within the brain tissue. The relative measurement sensitivity of the imaging probe at each voxel was defined as the maximum of the normalized Jacobians calculated across all source–detector pairs. The measurement field of view (FOV) was defined to include the voxels where the relative sensitivity was greater than 0.01 in all subjects (Fig. 4a). The statistical analysis of the reconstructed images was limited to GM voxels within the FOV.

2.11. Region-of-interest analysis

In line with our hypotheses, we selected two regions of interest (ROIs) delineated in the age-appropriate Automated Anatomical labelling (AAL) template published by Shi et al. (2011). Olausson et al. (2002) studied an adult subject who lacked Aβ afferents but had intact CT afferents as a result of sensory neuronopathy, along with healthy controls, using fMRI. Slow strokes of 2–10 cm/s on the right forearm were used to activate CT afferents. On the contralateral hemisphere, the insular cortex and premotor cortex (PMC) had significant activation in the patient, while S1 or S2 were not activated. In some of the controls, S1, S2, insula, and PMC were activated. Morrison et al. used 3 and 30 cm/s brushing on the left forearm and imaged adult subjects using fMRI (Morrison et al., 2011). They reported slow > fast in a region of the posterior insula, superior parietal cortex and postcentral gyrus. In two-month-old infants, Jönsson et al. reported statistically significant slow > fast responses in the insula, using DOT (Jönsson et al., 2018). Pirazzoli et al. reported significant responses to affective touch in the left inferior frontal gyrus (IFG) and posterior superior temporal sulcus (STS) in 5-month infants using fNIRS (Pirazzoli et al., 2019). Davidovic et al. reported responses to 2 cm/s brushing in the left postcentral gyrus (PoCG-L), superior frontal gyrus (SFG-L), left IFG, precentral gyrus (PreCG-L), and lentiform gyrus (outside of FOV) using fMRI in adults (Davidovic et al., 2016). Based on these considerations, we selected three ROIs, ROI 1 is AAL 29 (left insula, INS-L), ROI 2 is AAL 57 (left postcentral gyrus, location of the primary somatosensory cortex, PoCG-L) and ROI 3 is AAL 11 (IFGoperc-L). PMC, S2 and pSTS were not used as ROIs because these regions are not defined in the template and the precise location of pSTS varies from study to study in the literature.

The HbT response amplitudes for the GM voxels within the FOV were averaged within each ROI. The statistical significance of the difference between HbT response amplitudes between the two conditions (slow vs. fast brushing) and the difference between each condition and baseline was assessed using Student's t-test. Multiple comparison correction was applied using the Bonferroni method for $N = 3$ regions.

2.12. Clustering based on voxel-level statistics

In the second analysis approach, we consider an alternative delineation of activated or deactivated regions that is not dependant on the anatomical parcellation of the atlas. We first calculate the voxel-level statistical significance of the responses and merge adjacent voxels that show sufficient statistical significance into clusters. We start by combining adjacent GM voxels that satisfy $p_{\mathrm{voxel}} < p_{\mathrm{th,L1}} = 0.001$ into clusters and calculate the cluster average HbT response for each condition. The voxel-level significance threshold is then increased to $p_{\mathrm{th,L2}} = 0.033$ and $p_{\mathrm{th,L3}} = 0.01$ and the clusters are extended to include these additional adjacent voxels. The cluster statistical significance is compared between

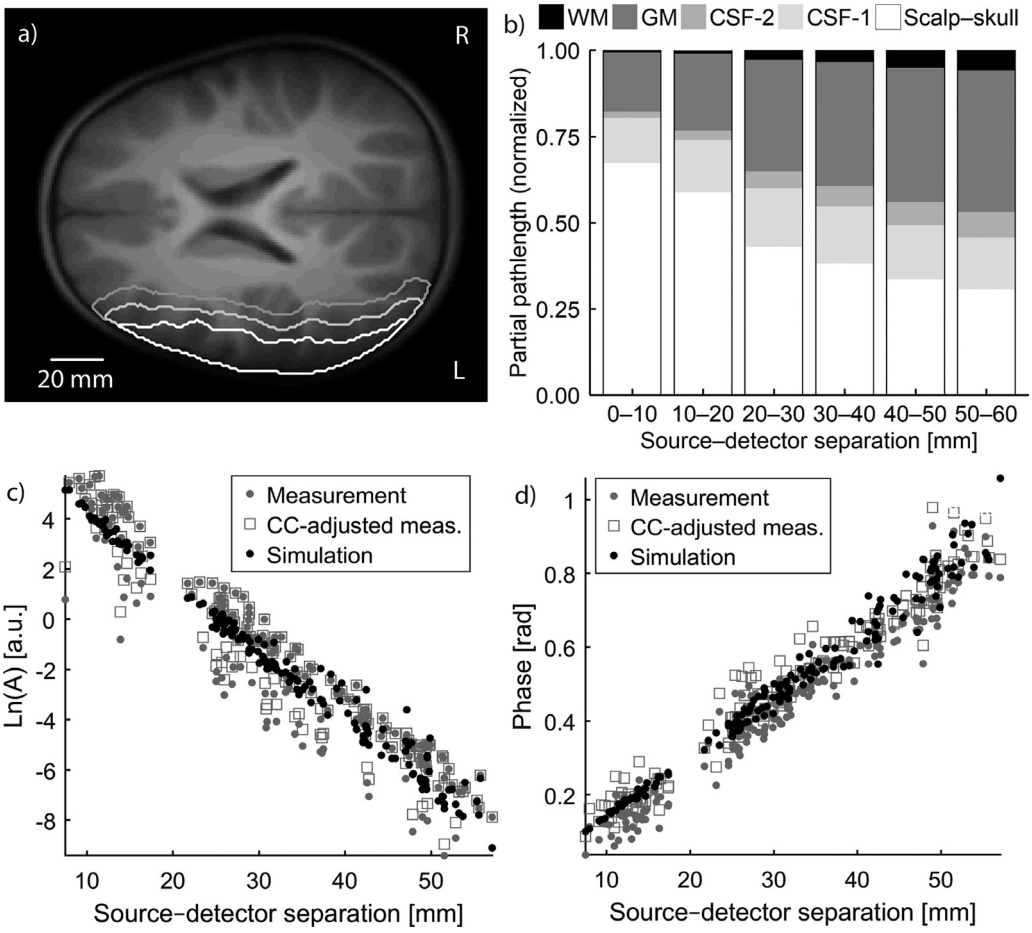

Fig. 4. Measurement sensitivity and parameter fitting. a) Approximate sensitivity of the measurement probe displayed as contour map overlaid on an axial slice of the anatomical template. The relative sensitivity exceeds 0.1 inside the white line (light grey line 0.01,dark grey line 0.001). b) Bar graph illustrating the relative partial pathlengths in each tissue type for different source–detector separations (SDSs). White = combined scalp and skull layer, light grey = CSF-1 = subarachnoid CSF, mid-grey = CSF-2 = low-scattering CSF in the sulci and ventricles, dark grey = grey matter (GM), black = white matter (WM). c) For one subject, the simulated, measured, and coupling coefficient (CC)-adjusted log amplitude data. d) Simulated, measured and CC-adjusted phase data. The simulated data in c) and d) were calculated using MCX and the optical properties in Table 2.

voxel-wise significance levels L1, L2, and L3 and the cluster extent is determined based on the smallest p-value where the minimum volume threshold is satisfied. In principle, a larger number of threshold levels could be considered but for practical reasons we limited the analysis to three levels.

The cluster-wise averages are compared between slow brushing vs. baseline, fast brushing vs. baseline and slow vs. fast brushing using Student's t-test. The Bonferroni method was used to correct for multiple comparisons due to the number of regions tested. The correction factor was determined based on the following considerations: First, we calculated the number of grey matter voxels within the FOV of the probe $N_{GM,\,FOV} = 66 \times 10^3$. We consider that the imaging method is able to delineate approximately regions of 1 cm^3 from each other. Thus, the number of regions is $N_{MC,1} = 66$. We also calculated the number of source–detector pairs for which $12 < SDS <= 55$ as $N_{MC,2} = 151$. The larger of these two (151) was selected as the correction factor in the clustering based on voxel-level statistics.

A minimum cluster size of 50 voxels (in the original atlas template, this corresponds to 50 mm^3) was set to control the false positive rate of the clustering method. The threshold was chosen using a validation procedure where a large quantity of synthetic resting-state data was generated and processed through the analysis pipeline. A false positive rate of 0.05 was observed with a 50-voxel minimum cluster size. This approach is conceptually similar to Salli et al. (2001) and Cox et al. (2017).

The statistical power was not estimated prior to the analysis as the optical properties and functional contrast were not adequately known until a late stage in the analysis.

2.13. Data and code availability

Data recorded and analysed in the study are available upon contacting the corresponding author with a reasonable request. The data sharing will be subject to the limitations specified in the consent form and Finnish law. Analysis code can be made available subject to an agreement between the parties and Aalto University.

3. Results

3.1. Optical parameters

The optical properties obtained from the fitting procedure described in Section 2.8 as the set of parameters which minimized the sum of rankings over all subjects are presented in Table 2.

Fig. 4a illustrates the region where the relative sensitivity is greater than 0.1, 0.01, and 0.001 for all subjects. The FOV was defined as the region inside the 0.01 line. The mean partial pathlengths of the detected photons for each source–detector range and each tissue type using the final optical parameters are illustrated in the bar graph in Fig. 4b. The

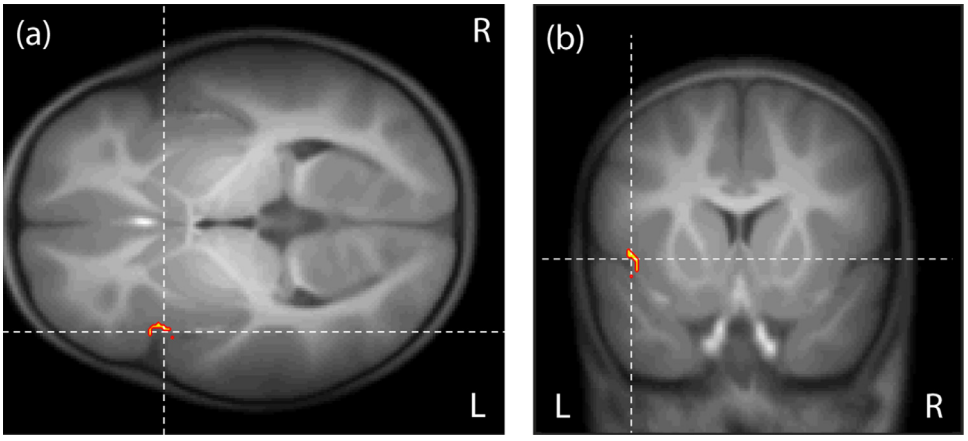

Fig. 5. Results from region of interest -based analysis. a) Axial and b) coronal slices of the template with AAL region 29 (INS-L) where the HbT response to slow brushing is greater than to fast brushing (slow > fast; p = 0.01). Voxels within the FOV indicated in yellow. (Table 3) (Figure should be printed in colour.).

Table 3
Response magnitudes and statistical significance in regions of interest (ROIs). p-values given uncorrected. * = $p < 0.05$ (uncorrected); ** = $p < 0.05$ corrected for multiple comparisons (3) using the Bonferroni method. INS-*L* = insula left.

AAL region	Location	N_{vox}	Slow	Fast	Slow-Fast
ROI 1 AAL 29 Fig. 5ab	INS-L	105	0.20 μM	−0.96 μM	1.2 μM** $p = 0.01$**

Table 4
Voxel statistics -based clustering results. The uncorrected p-values are given in this table. * = $p < 0.05$ (uncorrected); ** = $p < 0.05$ corrected for multiple comparisons (151) with the Bonferroni method. PoCG-*L* = precentral gyrus left, ROL-*L* = Rolandic operculum left, STG-*L* = superior temporal gyrus left.

Cluster	Location	N_{vox}	Slow	Fast	Slow-Fast
C1 (L2) Fig. 6ab	57 PoCG-L 55% 17 ROL-L 27% 81 STG-L 18%	85	−1.2 μM	1.4 μM	−2.6 μM** $p = 2.3 \times 10^{-4}$**

tissue-wise partial pathlengths for each detected photon were computed with MCX (see Section 2.9) and normalized for each source–detector pair by dividing the sum of the weighted partial pathlengths by the sum of the weighted total pathlengths. The normalized values were then averaged over each SDS range and over all 16 subjects. At SDS ≤ 10 mm, 67% of the pathlength is in the scalp + skull layer, and 17% in GM. At SDS > 50 mm, 31% of the pathlength is in the scalp + skull layer and 41% in the GM. The mean partial pathlength in WM is 1–6%. Fig. 4c and 4d illustrate the fit between the simulated, measured, and CC-adjusted measured ln(A) and phase, respectively, using the final optical parameters for one subject.

3.2. Touch responses based on region-of-interest (ROI) analysis

In ROI 1 (INS-L), 105 voxels were within the FOV of the probe. The HbT response to slow brushing was statistically significantly greater than the response to fast brushing (slow – fast = 1.2 μM; slow > fast; $p = 0.01$; Table 3; Fig. 5a-b).

3.3. Touch responses based on voxel-level clustering

A statistically significant difference between the HbT responses to slow and fast brushing was found (slow – fast = −2.6 μM; fast > slow; $p = 2.3 \times 10^{-4}$; $p_{Bonf} = 0.03$; Table 4; Fig. 6a-b) in a 85-voxel cluster (C1) residing in the Postcentral Gyrus (PoCG-L), Rolandic Operculum (ROL-L) and Superior Temporal Gyrus (STG-L). This is part of the primary somatosensory cortex (SI).

4. Discussion

4.1. Affective and non-affective touch processing

In the present study, we investigated the processing of affective and non-affective touch in two-year-old children using diffuse optical tomography (DOT). We applied affective touch (represented by CT-optimal brushing at 3 cm/s) and non-affective touch (represented by non-CT-optimal 30 cm/s brushing) to the right forearm and imaged total haemoglobin (HbT) responses on the left hemisphere. We found statistically significant differences in HbT responses between slow and fast brushing in two regions: slow > fast in the insula and fast > slow in a cluster residing in the postcentral gyrus, Rolandic operculum and superior temporal gyrus. Insula activation in response to CT-optimal stimulation is consistent with fMRI findings in adult subjects (Olausson et al., 2002). The primary somatosensory cortex (S1) is activated by discriminative touch. Our present findings in two-year-olds are consistent with the theory of opposite effects of CT afferent stimulation in insula and S1 presented by Olausson et al. (2008) and in McGlone et al. (2012). CT-optimal stimulation was reported to deactivate S1 in Aβ-deafferented adult subjects (Olausson et al., 2008) and cause no statistically significant response in the contralateral S1 in healthy controls (Olausson et al., 2002). The fast > slow cluster of the present study is located inferiorly to the expected representative area of the arm in S1; this may be in part because it is near the edge of the field-of-view (FOV) of the probe.

In a previous study on two-month-old infants, we found the HbT response to slow brushing to be greater than fast brushing (slow > fast) in the insula and a statistically weaker slow > fast in middle temporal cortex (Jönsson et al., 2018). This is consistent with our present findings in two-year-old subjects. Although previous research indicates that the primary somatosensory cortex (S1) is primarily involved in non-affective touch processing in adults (Cohen et al., 1991; Knecht et al., 2003; Tegenthoff et al., 2005; Lundblad et al., 2011), a few recent studies suggest that S1 may be involved in processing affective touch as well (Gazzola et al., 2012; McCabe et al., 2008; Tuulari et al., 2019). Tuulari et al. studied fMRI blood oxygen level dependant (BOLD) responses to affective touch (applied by slow brushing on the right leg of the infant) in one-month-old infants and found significant positive responses in the insula and the postcentral gyrus (Tuulari et al., 2019). In the present study, we found fast > slow in an area residing in the inferior postcentral gyrus, Rolandic operculum and superior temporal gyrus, which may be reflective of preferential processing of non-affective touch in S1. This is in contrast to Jönsson et al., where fast > slow responses were not found in two-month-old infants in S1 although the FOV of the probe included more superior areas than in the present study (Jönsson et al., 2018). This suggests that the processing of discriminative touch might not be fully developed at two months of age (Jönsson et al., 2018) but

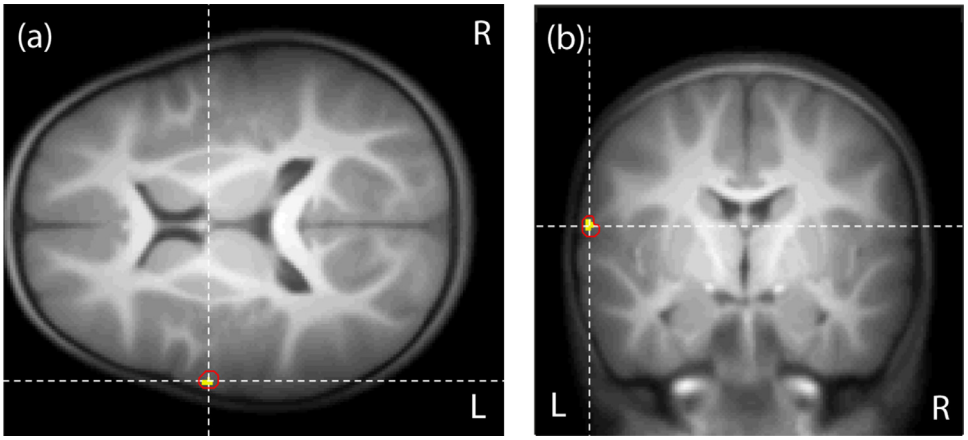

Fig. 6. Results from cluster analysis. a) Axial and b) coronal slices of C1 in the Postcentral Gyrys, Rolandic Operculum and Superior Temporal Gyrus where the HbT response to fast brushing is greater than to slow brushing (fast > slow; $p_{Bonf} < 0.03$). $p_{voxel} < 0.001$ indicated in yellow; $p_{voxel} = 0.01$ contour marked with red line. (Table 4) (Figure should be printed in colour.).

may be more mature at two years of age. S1 responses to affective touch at one month of age reported in Tuulari et al. may have benefited from the greater FOV of fMRI but also the stimulation site was different (foot vs. arm) (Tuulari et al., 2019).

In the fNIRS study by Pirazzoli et al. (2019), affective and non-affective touch were applied to the forearm of 5-month-old infants and significant positive responses to affective touch were found in the inferior frontal gyrus (IFG) and posterior superior temporal sulcus (pSTS). However, the differences between affective and non-affective touch were not statistically significant. In our present study, we also found no statistically significant differences between slow and fast brushing in the opercular IFG based on the current group-level analysis. It is possible that DOT with 3D reconstruction gives a different interpretation to the location of the responses, wherein the most significant response for affective touch is in the insula instead of, e.g., the IFG or STS. This does not, however, exclude the possible involvement of these areas in the processing of affective touch.

4.2. Clinical relevance

Clinically, affective touch processing has been investigated not only in typically-developing children but also in children with disrupted social perception, such as autism spectrum disorder (ASD). Using fMRI, Kaiser et al. found children with ASD (aged 5–17 years) to have disrupted processing of CT-targeted touch in areas normally involved in processing social and emotional information including the insula, ventrolateral prefrontal cortex, temporal pole, STS, temporoparietal junction, inferior parietal lobule, amygdala, fusiform gyrus and IFG, whereas responses to non-CT-targeted touch were enhanced in S1 and insula, relative to typically-developing children (Kaiser et al., 2016). Using DOT, it is possible to observe the development of a child's processing of affective touch and detect atypical responses which may be relevant to the social development and mental health of the child.

4.3. Modelling of light propagation in a realistic model of the child's head

DOT difference imaging can tolerate some inaccuracy in the forward model in the tissue-specific optical parameters, optode positions, and boundary shape due to the partial cancellation of errors when the differences in data are calculated between resting and active states (Hillman et al., 2000; Heiskala et al., 2009a; Mozumder, 2015). However, large errors in background optical properties do tend to result in inaccurate reconstruction of the dynamic changes inside the tissue. In the case of activation in deeper cortical tissue such as the insula, the optical properties of the tissue model have a significant impact on the reconstruction.

Our approach of fitting the optical parameters by comparing MC simulated data from an atlas model with two separate CSF types to FD measurements from a high-density optode array with coupling coefficient corrections is novel. Many previous studies on human head parameter estimation from FD or TD data have used simple head models, such as homogeneous semi-infinite slabs and spheres or two-layered slabs, to enable solving either the coefficients or the forward problem analytically (Bevilacqua et al., 1999; Zhao et al., 2005; Dehaes et al., 2011; Hallacoglu et al., 2013; Farina et al., 2015; Farzam et al., 2017). For example, Franceschini et al. studied infant brain oxygen saturation (StO_2), blood volume (CBV), and HbT through the infant's first year of life using FD, multidistance NIRS with the assumption of tissue homogeneity (Franceschini et al., 2007). Ijichi et al. measured the optical properties of neonates using time-resolved spectroscopy (Ijichi et al., 2005). Estimation of parameters in realistic anatomical models (but with fewer than five tissue types) has often been based on time domain data where one can compare the measured and simulated time point spread functions (TPSF) (Barnett et al., 2003; Gagnon et al., 2008; Selb et al., 2014; Mahmoodkalayeh et al., 2019).

As a result of the improved accuracy of modelling of the optical structure of the two-year-old subjects' head, we were able to localize the primary activation due to CT afferent stimulation in the insula, consistent with fMRI (Olausson et al., 2002, 2008) and DOT in infants (Jönsson et al., 2018). Further improvement in accuracy of forward modelling might be achieved by allowing some heterogeneity within each tissue type by making a softer spatial prior based on the atlas. The unconstrained reconstruction of the spatial distribution of optical properties suffers from reduced contrast due to the partial volume effect (Nissilä et al., 2005a; Schweiger et al., 2005). Both quantitative and spatial accuracy can be improved by increasing the number of optodes covering a given area (Heiskala et al., 2009a). By utilizing structural prior information in the fitting, the contrast loss that occurs in free-form reconstruction is reduced. Other approaches that have been suggested to improve quantitative accuracy include classification-based methods (Hiltunen et al., 2009) and level-set reconstruction (Schweiger et al., 2010).

The selected literature-based properties for the two CSF compartments and WM can affect the fitted estimates for SS and GM. The measurement sensitivity to WM properties in this geometry is considered low due to the on average 1–6% partial pathlengths predicted by the forward model. Use of individual best-fit optical properties would enable accounting for individual features such as skin and hair colour. To make the fitting more robust at the individual subject level, shorter SDS measurements and each subject's own MR images would be helpful for more accurate modelling of the thickness of the superficial layers (Mahmoodkalayeh et al., 2019) and the location and size of the CSF pools which are important for accurate modelling of light propagation.

4.4. Limitations of the study

Triscoli et al. (2013) found that the subject-reported pleasantness of brushing stimuli delivered manually at 3 cm/s is comparable to that of analogous stimulation delivered by a robot. However, the use of a robot to apply the brushing to the subject's forearm would have required the subject to hold their arm still during the entire session, which was not realistic with two-year-old subjects. Therefore, the touch stimuli were provided using a hand-held brush to make the stimulation more natural and the subject as comfortable as possible. We selected the duration of the touch stimuli as two seconds to administer the stimuli in a controlled and reproducible manner and so that it is short enough that an adequate number of repetitions could be presented. During the measurement session, the child was watching a neutral cartoon video. While we cannot rule out the possibility that watching the video alters brain processing during the presentation of the touch stimuli; since the video is not synchronized with the stimulus presentation, it is unlikely that this would alter the essential characteristics of the results.

Our measurement probe covered about one-half of the superficial cortical surface of the left hemisphere, and some regions relevant to affective touch processing were excluded because of this. Regions which were not included within the FOV but are sometimes reported activated (or connected to areas activated) in response to affective touch in fMRI studies on adult subjects are the right S2, the right posterior superior temporal sulcus (pSTS), and the right orbitofrontal cortex (OFC) as well as deep brain areas such as the anterior cingulate gyrus (ACC), striatum, amygdala and cerebellum (Rolls 1999; Rolls et al., 2001; Olausson et al., 2002; Rolls et al., 2003; McGlone et al., 2012; Gordon et al., 2013). In addition, the superior parts of the prefrontal cortex (PFC) and S1 are not within the FOV. The OFC is thought to be involved in complex emotional processing and receives inputs from the insula and outputs to the ACC (Rolls 1999; Rolls et al., 2003; Rolls 2019). The dorsal ACC and medial PFC are found activated by affective touch and connected to the insula and amygdala (Gordon et al., 2013). The OFC activity during affective touch is modulated by oxytocin (Chen et al., 2020) and the ACC contains receptors for opioids (Lindgren et al., 2012). The amygdala is involved in emotional processing (Adolphs 2010) and the striatum and ACC are part of the "reward circuit" of the brain (McGlone et al., 2014). This means that affective touch is processed in a distributed network in the brain. However, despite these limitations, the most consistently reported regions are the contralateral insula, S1 and S2 which were within our setup's FOV. We believe that many interesting phenomena associated with affective touch processing can be imaged by further developing the optical imaging technique which is less demanding of the child than fMRI.

We assumed the time course of the haemodynamic response to follow a slightly delayed canonical model of a haemodynamic response function to focus the analysis on the early phase of the event-related haemodynamic responses rather than subsequent processing. An age-appropriate atlas was deformed to match each subject's head shape as anatomical images for each individual subject were not available. The optical properties for each tissue compartment were assumed to be constant and additionally the white matter and cerebrospinal fluid optical properties were assumed from the literature. The grey matter and skin & skull parameters which gave the best overall fit across the subjects were used instead of individual best-fit parameters. This made the fitting procedure more robust but does not account for inter-individual variations or inhomogeneities in the optical properties within tissue compartments.

4.5. Future views

A recent development in DOT and fNIRS neuroimaging instrumentation is the development of fibreless and/or wireless instruments that can be worn on the subject's head without a large number of cables in the headgear (Pinti et al., 2018). This approach has many advantages in a clinical monitoring environment as well as for neuroimaging children. The subjects can play and interact socially with others during the session without the instrument or cables getting in the way, which can lead to more realistic and naturalistic imaging of brain activity. However, given the present findings, we encourage researchers working in the field to collect some measurements with time- or frequency-domain instruments and confirm that the optical properties that they use in their model are accurate for the subject population.

Conclusion

Touch plays a crucial role in forming social bonds, especially in parent-child interaction, and thus it is important to understand the neural mechanisms of tactile processing in children. Our study is the first to demonstrate differential processing of affective and non-affective touch in the left insula as well as the primary somatosensory cortex in two-year-old children and fills an important gap in the literature on affective touch processing in toddlers. Diffuse optical tomography (DOT) is suitable for imaging neural development in small children because it does not impose strict limitations on subject movement. Accurate modelling of light transport is critical for correct reconstruction of activity in deeper areas of the brain. The richer information provided by frequency-domain DOT proved itself invaluable in this context.

Declaration of Competing Interests

The authors declare no competing interests.

Credit authorship contribution statement

Ambika Maria: Conceptualization, Investigation, Data curation, Writing – original draft, Writing – review & editing, Funding acquisition. **Pauliina Hirvi:** Methodology, Software, Formal analysis, Writing – original draft, Writing – review & editing, Visualization, Funding acquisition. **Kalle Kotilahti:** Methodology, Software, Formal analysis, Investigation, Resources, Writing – review & editing. **Juha Heiskala:** Methodology, Software, Writing – review & editing. **Jetro J. Tuulari:** Writing – review & editing, Supervision. **Linnea Karlsson:** Conceptualization, Resources, Writing – review & editing, Supervision, Funding acquisition. **Hasse Karlsson:** Conceptualization, Resources, Writing – review & editing, Supervision, Project administration, Funding acquisition. **Ilkka Nissilä:** Conceptualization, Methodology, Software, Validation, Formal analysis, Investigation, Resources, Data curation, Writing – original draft, Writing – review & editing, Visualization, Supervision, Project administration, Funding acquisition.

Acknowledgements

We would like to thank all our participant families for their cooperation and time. We are grateful to Eija Jossandt and Jussi Kasurinen for helping with the data collection. IN would like to thank Dr. Johanna Metsomaa for her help with the validation of the clustering. Funding: This work was supported by the Academy of Finland (projects 269282 (to IN); 273451 and 303937 (to IN); 134950 (to HK); 253270 (to HK)), Jane and Aatos Erkko Foundation (to HK, LK), Signe and Ane Gyllenberg Foundation (to HK, LK), State Research Grant (EVO) (to HK, LK, JJT), Alfred Kordelin Foundation (to JJT) and the Vilho, Yrjö and Kalle Väisälä Foundation of the Finnish Academy of Science and Letters (to PH). The Monte Carlo simulations presented above were performed using computer resources within the Aalto University School of Science "Science-IT" project. The funding sources had no involvement in study design, collection, analysis or interpretation of data, in the writing of the report or the decision to submit the article for publication.

References

Ackerley, R., Backlund Wasling, H., Liljencrantz, J., Olausson, H., Johnson, R.D., Wessberg, J, 2014a. Human C-tactile afferents are tuned to the temperature of a skin-stroking caress. J. Neurosci. 34, 2879–2883.

Ackerley, R., Saar, K., McGlone, F., Wasling, H.B., 2014b. Quantifying the sensory and emotional perception of touch: differences between glabrous and hairy skin. Front. Behav. Neurosci. 8, 34. doi:10.3389/fnbeh.2014.00034.

Adolphs, R., 2010. What does the amygdala contribute to social cognition? Ann. NY Acad. Sci. 1191-42-61.

Arridge, S.R., 1999. Optical tomography in medical imaging. Inverse Probl. 15, R41.

Barnett, A.H., Culver, J.P., Sorensen, A.G., Dale, A., Boas, D.A., 2003. Robust inference of baseline optical properties of the human head with three-dimensional segmentation from magnetic resonance imaging. Appl. Opt. 42 (16), 3095–3108. doi:10.1364/AO.42.003095.

Bauer, J., Sontheimer, D., Fischer, C., Linderkamp, O., 1996. Metabolic rate and energy balance in very low birth weight infants during kangaroo holding by their mothers and fathers. J. Pediatr. 129 (4), 608–611. doi:10.1016/s0022-3476(96)70129-4.

Beauchamp, M.S., Beurlot, M.R., Fava, E., Nath, A.R., Parikh, N.A., Saad, Z.S., Bortfelt, H., Oghalai, J.S., 2011. The developmental trajectory of brain-scalp distance from birth through childhood: implications for functional neuroimaging. PLoS ONE 6, e24981.

Bennett, R.H., Bolling, D.Z., Anderson, L.C., Pelphrey, K.A., Kaiser, M.D., 2014. fNIRS detects temporal lobe response to affective touch. Soc. Cogn. Affect. Neurosci. 9 (4), 470–476. doi:10.1093/scan/nst008.

Bessou, P., Burgess, P.R., Perl, E.R., Taylor, C.B., 1971. Dynamic properties of mechanoreceptors with unmyelinated I fibers. J. Neurophysiol. 34 (1), 116–131.

Bevilacqua, F., Piguet, D., Marquet, P., Gross, J.D., Tromberg, B.J., Depeursinge, C., 1999. In vivo local determination of tissue optical properties: applications to human brain. Appl. Opt. 38 (22), 4939–4950.

Björnsdotter, M., Morrison, I., Olausson, H., 2010. Feeling good: on the role of C fiber mediated touch in interoception. Exp. Brain Res. 207 (3–4), 149–155. doi:10.1007/s00221-010-2408-y.

Björnsdotter, M., Gordon, I., Pelphrey, K.A., Olausson, H., Kaiser, M.D., 2014. Development of brain mechanisms for processing affective touch. Front. Behav. Neurosci. 8, 24. doi:10.3389/fnbeh.2014.00024.

Boas, David, 1996. Diffuse photon probes of structural and dynamical properties of turbid media: Theory and biomedical applicationsDiffuse photon probes of structural and dynamical properties of turbid media: Theory and biomedical applications. Dissertations available from ProQuest. AAI9636132.. https://repository.upenn.edu/dissertations/AAI9636132.

Brigadoi, S., Cooper, R.J., 2015. How short is short? Optimum source-detector distance for short-separation channels in functional near-infared spectroscopy. Neurophotonics 2, 025005.

Champagne, F.A., 2008. Epigenetic mechanisms and the transgenerational effects of maternal care. Front. Neuroendocrinol. 29, 386–397.

Chen, Y., Li, Q., Zhang, Q., Kou, J., Zhang, Y., Cui, H., m, Wernicke, J., Montag, C., Becker, B., Kendrick, K.M., Yao, S., 2020. Oxytocin increases the pleasantness of affective touch and orbitofrontal cortex activity independent of valence. Eur. Neuropsychopharmacol. 39, 99–110.

Christensson, K., 1996. Fathers can effectively achieve heat conservation in healthy newborn infants. Acta Paediatr. 85 (11), 1354–1360. doi:10.1111/j.1651-2227.1996.tb13925.

Cohen, L.G., Bandinelli, S., Sato, S., Kufta, C., Hallett, M., 1991. Attenuation in detection of somatosensory stimuli by transcranial magnetic stimulation. Electroencephalogr. Clin. Neurophysiol. /Evoked Potent. Sec. 81 (5), 366–376. doi:10.1016/0168-5597(91)90026-t.

Cope, M., 1991. The Development of a Near Infrared Spectroscopy System and its Application for Non-Invasive Monitoring of Cerebral Blood and Tissue Oxygenation in the Newborn Infant. University of London, London PhD Thesis.

Cox, R.W., Chen, G., Glen, D.R., Reynolds, R.C., Taylor, P.A., 2017. fMRI clustering and false-positive rates. Proc. Natl. Acad. Sci. USA 114, E3370–E3371. doi:10.1073/pnas.1614961114.

Culver, J.P., Siegel, A.M., Franceschini, M.A., Mandeville, J.B., Boas, D.A., 2005. Evidence that cerebral blood volume can provide brain activation maps with better spatial resolution than deoxynated haemoglobin. NeuroImage 27, 947–959.

Custo, A., Wells III, W.M., Barnett, A.H., Hillman, E.M.C., Boas, D.A, 2006. Effective scattering coefficient of the cerebral spinal fluid in adult head models for diffuse optical imaging. Appl. Opt. 45 (19), 4747–4755. doi:10.1364/AO.45.004747.

Custo, A., Boas, D.A., Tsuzuki, D., Dan, I., Mesquita, R., Fischl, B., Grimson, W.E.L., Wells III, W., 2010. Anatomical atlas-guided diffuse optical tomography of brain activation. NeuroImage 49, 561–567.

Chance, B., 1998. Phase measurement of light absorption and scatter in human tissue. Rev. Sci. Instrum. 69, 3457.

Davidovic, M., Jönsson, E.H., Olausson, H., Björnsdotter, M., 2016. Posterior superior temporal sulcus responses predict perceived pleasantness of skin stroking. Front. Hum. Neurosci. 10, 432. doi:10.3389/fnhum.2016.00432.

Dehaes, M., Grant, P.E., Sliva, D.D., Roche-Labarbe, N., Pienaar, R., Boas, D.A., Franceschini, M.A., Selb, J., 2011. Assessment of the frequency-domain multi-distance method to evaluate the brain optical properties: monte Carlo simulations from neonate to adult. Biomed. Opt. Express 2 (3), 552–567.

Deoni, S.C.L., O'Muircheartaigh, J., Elison, J.T., Walker, L., Doernberg, E., Waskiewicz, N., Dirks, H., Piryatinsky, I., Dean III, D.C., Jumbe, N.L., 2016. White matter maturation profiles through early childhood predict general cognitive ability. Brain Struct. Funct. 221, 1189–1203.

Devor, A., Tian, P., Nishimura, N., Teng, I.C., Hillman, E.M.C., Narayanan, S.N., Ulbert, I., Boas, D.A., Kleinfeld, D., Dale, A.M., 2007. Suppressed neuronal activity and concurred arteriolar vasoconstriction may explain negative blood oxygen level-dependent signal. J. Neurosci. 27 (16), 4452–4459. doi:10.1523/JNEUROSCI.0134-07.2007.

Dunbar, R., 2010. The social role of touch in humans and primates: behavioural function and neurobiological mechanisms. Neurosci. Biobehav. Rev. 34, 260–268. doi:10.1016/j.neubiorev.2008.07.001.

Erlandsson, K., Dsilna, A., Fagerberg, I., Christensson, K., 2007. Skin-to-skin care with the father after cesarean birth and its effect on newborn crying and prefeeding behaviour. Birth 34 (2), 105–114. doi:10.1111/j.1523-536x.2007.00162.

Fairhurst, M. T., Löken, L., Grossmann, T., 2014. Physiological and Behavioral Responses Reveal 9-Month-Old Infants' Sensitivity to Pleasant Touch. Psychological Science 25, 1124–1131.

Faizy, T.D., Kumar, D., Broocks, G., Thaler, C., Flottmann, F., Leischner, H., Kutzner, D., Hewera, S., Dotzauer, D., Stellmann, J.-.P., Reddy, R., Fiehler, J., Sedlacik, J., Gellissen, S., 2018. Age-related measurements of the myelin water fraction derived from 3D multi-echo GRASE reflect myelin content of the cerebral white matter. Sci. Rep. 8, 14991.

Fang, Q., Boas, D.A., 2009a. Tetrahedral mesh generation from volumetric binary and grayscale images. 2009 IEEE International Symposium on Biomedical Imaging: From Nano to Macro doi:10.1109/isbi.2009.5193259.

Fang, Q., Boas, D.A., 2009b. Monte Carlo simulation of photon migration in 3D turbid media accelerated by graphics processing units. Opt. Express 17, 20178–20190.

Farina, A., Torricelli, A., Bargigia, I., Spinelli, L., Cubeddu, R., Foschum, F., Jäger, M., Simon, E., Fugger, O., Kienle, A., Martelli, F., Di Ninni, P., Zaccanti, G., Milej, D., Sawosz, P., Kacprzak, M., Liebert, A., Pifferi, A., 2015. In-vivo multilaboratory investigation of the optical properties of the human head. Biomed. Opt. Express 6, 2609–2623.

Farzam, P., Buckley, E.M., Lin, P.-.Y., Hagan, K., Grant, P.E., Inder, T.E., Carp, S.A., Franceschini, M.A., 2017. Shedding light on the neonatal brain: probing cerebral hemodynamics by diffuse optical spectroscopic methods. Sci. Rep. 7, 1–10.

Feldman, R., Singer, M., Zagoory, O., 2010. Touch attenuates infants' physiological reactivity to stress. Dev. Sci. 13, 271–278. doi:10.1111/j.1467-7687.2009.00890.

Feldman, R., Eidelman, A.I., 2004. Parent–infant synchrony and the social-emotional development of triplets. Dev. Psychol. 40, 1133–1147.

Feldman, R., Eidelman, A.I., 2003. Direct and indirect effects of maternal milk on the neurobehavioral and cognitive development of premature infants. Dev. Psychobiol. 43, 109–119.

Ferradal, S.L., Eggebrecht, A.T., Hassanpour, M., Snyder, A.Z., Culver, J.P., 2014. Atlas-based head odelling and spatial normalization for high-density diffuse optical tomography: in vivo validation against fMRI. NeuroImage 85, 117–126.

Firbank, M., Hiraoka, M., Essenpreis, M., Delpy, D.T., 1993. Measurement of the optical properties of the skull in the wavelength range 650-950nm. Phys. Med. Biol. 38, 503.

Franceschini, M.A., Thaker, S., Themelis, G., Krishnamoorthy, K., Bortfeld, H., Diamond, S.G., Boas, D.A., Arvin, K., Grant, P.E, 2007. Assessment of infant brain development with frequency-domain near-infrared spectroscopy. Pediatr. Res. 61, 546–551.

Frisch, D., 2018. point2trimesh.m — distance between point and triangulated surface. MATLAB Central File Exchange. https://www.mathworks.com/matlabcentral/fileexchange/52882-point2trimesh-distance-between-point-and-triangulated-surface (Accessed 20 April 2018).

Fukui, Y., Ajichi, Y., Okada, E., 2003. Monte Carlo prediction of near-infrared light propagation in realistic adult and neonatal head models. Appl. Opt. 42, 2881–2887.

Gagnon, L., Gauthier, C., Hoge, R.D., Lesage, F., Selb, J.J., Boas, D.A., 2008. Double-layer estimation of intra- and extracerebral hemoglobin concentration with a time-resolved system. J. Biomed. Opt. 13 (5), 1–9.

Gagnon, L., Yücel, M.A., Dehaes, M., Cooper, R.J., Perdue, K.L., Selb, J., Huppert, T.J., Hoge, R.D., Boas, D.A., 2012. Quantification of the cortical contribution to the NIRS signal over the motor cortex using concurrent NIRS-fMRI measurements. NeuroImage 59, 3933–3940.

Gallace, A., Spence, C., 2010. The science of interpersonal touch: an overview. Neurosci. Biobehav. Rev. 34 (2), 246–259. doi:10.1016/j.neubiorev.2008.10.004.

Gazzola, V., Spezio, M.L., Etzel, J.A., Castelli, F., Adolphs, R., Keysers, C., 2012. Primary somatosensory cortex discriminates affective significance in social touch. Proc. Natl. Acad. Sci. U.S.A. 109, E1657–E1666. doi:10.1073/pnas.1113211109.

Gibson, A.P., Riley, J., Schweiger, M., Hebden, J.C., Arridge, S.R., Delpy, D.T., 2003. A method for generating patient-specific finite element meshes for head modelling. Phys. Med. Biol. 48, 481–495. doi:10.1088/0031-9155/48/4/305.

Gibson, A.P., Austin, T., Everdell, N.L., Schweiger, M., Arridge, S.R., Meek, J.H., Wyatt, J.S., Delpy, D.T., Hebden, J.C, 2006. Three-dimensional whole-head optical tomography of passive motor evoked responses in the neonate. Neuroimage 30, 521–528.

Gordon, I., Voos, A.C., Bennett, R.H., Bolling, D.Z., Pelphrey, K.A., Kaiser, M.D., 2013. Brain mechanisms for processing affective touch. Hum. Brain Mapp. 34, 914–922. doi:10.1002/hbm.21480.

Gottlieb, G., Tobach, E., Aronson, L.R., Shaw, E., 1971. Ontogenesis of sensory function in birds and mammals. In: The Biopsychology of Development. Academic Press, New York, pp. 67–128.

Hallacoglu, B., Sassaroli, A., Fantini, S., 2013. Optical characterization of two-layered turbid media for non-invasive, absolute oximetry in cerebral and extracerebral tissue. PLoS ONE 8, e64095.

Harlow, H.F., 1958. The nature of love. Am. Psychol. 13, 673–685. doi:10.1037/h0047884.

Heiskala, J., Neuvonen, T., Grant, P.E., Nissilä, I., 2007a. Significance of tissue anisotropy in optical tomography of the infant brain. Appl. Opt. 46 (10), 1633–1640.

Heiskala, J., Kotilahti, K., Lipiäinen, L., Hiltunen, P., Grant, P.E., Nissilä, I., 2007b. Optical tomographic imaging of activation of the infant auditory cortex using perturbation Monte Carlo with anatomical a priori information. In: Diffuse Optical Imaging in Tissue B. W. Pogue and R. Cubeddu, eds. Proc. SPIE 6629, paper 66290T.

Heiskala, J., Hiltunen, P., Nissilä, I., 2009a. Significance of background optical properties, time-resolved information and optode arrangement in diffuse optical imaging of term neonates. Phys. Med. Biol. 54 (3), 535.
Heiskala, J., Pollari, M., Metsäranta, M., Grant, P.E., Nissilä, I., 2009b. Probabilistic atlas can improve reconstruction from optical imaging of the neonatal brain. Opt. Expr. 17, 14977–14992.
Heiskala, J., 2009c. Accurate Modelling of Tissue Properties in Diffuse Optical Imaging of the Human Brain. Helsinki University of Technology Ph.D. thesis https://aaltodoc.aalto.fi/handle/123456789/4655 .
Hillman, E.M.C., Hebden, J.C., Schmidt, F.E.W., Arridge, S.R., Schweiger, M., Dehghani, H., Delpy, D.T., 2000. Calibration techniques and datatype extraction for time-resolved optical tomography. Rev. Sci. Instrum. 71, 3415.
Hillman, E.M.C., Devor, A., Bouchard, M., Dunn, A.K., Krauss, G.W., Skoch, J., Bacskai, B.J., Dale, A.M., Boas, D.A., 2007. Depth-resolved optical imaging and microscopy of vascular compartment dynamics during somatosensory stimulation. Neuroimage 35, 89–104.
Hiltunen, P., Prince, S. J. D., Arridge, S., 2009. A combined reconstruction–classification method for diffuse optical tomography. Phys. Med. Biol. 54, 6457–6476.
Hirvi, P., 2019. Generating head models for diffuse optical tomography of the child brain. Master's Thesis. Aalto University https://aaltodoc.aalto.fi/handle/123456789/36377.
Hofer, M.A., 1995. Hidden regulators: implications for a new understanding of attachment, separation, and loss. In: Golberg, S., Muir, R., Kerr, J. (Eds.), Attachment theory: Social, developmental, and Clinical Perspectives. Analytic Press, Hillsdale, NJ, pp. 203–230.
Ijichi, S., Kusaka, T., Isobe, K., Okubo, K., Kawada, K., Namba, M., Okada, H., Nishida, T., Imai, T., Itoh, S., 2005. Developmental changes of optical properties in neonates determined by near-infrared time-resolved spectroscopy. Pediatr. Res. 58, 568–573.
Jönsson, E.H., Kotilahti, K., Heiskala, J., Wasling, H.B., Olausson, H., Croy, I., Mustaniemi, H., Hiltunen, P., Tuulari, J.J., Scheinin, M.N., Nissilä, I., 2018. Affective and non-affective touch evoke differential brain responses in 2-month-old infants. Neuroimage 169, 162–171. doi:10.1016/j.neuroimage.2017.12.024.
Kaiser, M.D., Yang, D.Y.-J., Voos, A.C., Bennett, R.H., Gordon, I., Pretzsch, C., Beam, D., Keifer, C., Eibott, J., McGlone, F., Pelphrey, A.K., 2016. Brain mechanisms for processing affective (and nonaffective) touch are atypical in autism. Cereb. Cortex 26, 2705–2714. doi:10.1093/cercor/bhv125.
Karlsson, L., Tolvanen, M., Scheinin, N.M., Uusitupa, H.M., Korja, R., Ekholm, E., Tuulari, J.J., Pajulo, M., Huotilainen, M., Paunio, T., Karlsson, H., 2018. Cohort profile: the FinnBrain birth cohort study (FinnBrain). Int. J. Epidemiol. doi:10.1093/ije/dyx173.
Knecht, S., Ellger, T., Breitenstein, C., Ringelstein, E.B., Henningsen, H., 2003. Changing cortical excitability with low-frequency transcranial magnetic stimulation can induce sustained disruption of tactile perception. Biol. Psychiatry 53 (2), 175–179. doi:10.1016/s0006322302013823.
Koikkalainen, J., Lötjönen, J., 2004. Reconstruction of 3-D head geometry from digitized point sets: an evaluation study. IEEE Trans. Inf. Technol. Biomed. 8 (3), 377–386.
Liao, S.M., Ferradal, S.L., White, B.R., Gregg, N., Inder, T.E., Culver, J.P., 2012. High-density diffuse optical tomography of term infant visual cortex in the nursery. J. Biomed. Opt. 17 (8), 081414. doi:10.1117/1.JBO.17.8.081414.
Lindgren, L., Westling, G., Brulin, C., Lehtipalo, S., Andersson, M., Nyberg, L., 2012. Pleasant human touch is represented in the pregenual anterior cingulate cortex. Neuroimage 59, 3427–3432.
Lindquist, M.A., Meng Loh, J., Atlas, L.Y., Wager, T.D, 2009. Modeling the hemodynamic response function in fMRI: efficiency, bias and mis-modeling. Neuroimage 45, S187–S198.
Lloyd-Fox, S., Blasi, A., Elwell, C.E., 2010. Illuminating the developing brain: the past, present and future of functional near infrared spectroscopy. Neurosci. Biobehav. Rev. 34 (3), 269–284. doi:10.1016/j.neubiorev.2009.07.008.
Lundblad, L.C., Olausson, H.W., Hermansson, A., Wasling, H.B., 2011. Cortical processing of tactile direction discrimination based on spatiotemporal cues in man. Neurosci. Lett. 501 (1), 45–49. doi:10.1016/j.neulet.2011.06.040.
Löken, L.S., Wessberg, J., Morrison, I., McGlone, F., Olausson, H., 2009. Coding of pleasant touch by unmyelinated afferents in humans. Nat. Neurosci. 12, 547–548. doi:10.1038/nn.2312.
Mahmoodkalayeh, S., Ansari, M.A., Tuchin, V.V., 2019. Head model based on the shape of the subject's head for optical brain imaging. Biomed. Opt. Express 10, 2795–2808.
Maria, A., Nissilä, I., Shekhar, S., Kotilahti, K., Tuulari, J. J., Hirvi, P., Huotilainen, M., Heiskala, J., Karlsson, L., Karlsson, H., 2020. Relationship between maternal pregnancy-related anxiety and infant brain responses to emotional speech – a pilot study. Journal of Affective Disorders 262, 62–70.
Maria, A, Shekhar, S., Nissilä, I., Kotilahti, K., Huotilainen, M., Karlsson, L., Karlsson, H., Tuulari, J. J., 2018. Emotional processing in the first two years of life: a review of near-infrared spectroscopy studies. J. Neuroimaging 28, 441–454.
McCabe, C., Rolls, E.T., Bilderbeck, A., McGlone, F., 2008. Cognitive influences on the affective representation of touch and the sight of touch in the human brain. Soc. Cogn. Affect. Neurosci. 3 (2), 97–108. doi:10.1093/scan/nsn005.
McGlone, F., Olausson, H., Boyle, J.A., Jones-Gotman, M., Dancer, C., Guest, S., Essick, G., 2012. Touching and feeling: differences in pleasant touch processing between glabrous and hairy skin in humans. Eur. J. Neurosci. 35 (11), 1782–1788. doi:10.1111/j.1460-9568.2012.08092.
McGlone, F., Wessberg, J., Olausson, H., 2014. Discriminative and affective touch: sensing and feeling. Neuron 82 (4), 737–755. doi:10.1016/j.neuron.2014.05.001.
Meaney, M.J., 2001. Maternal care, gene expression, and the transmission of individual differences in stress reactivity across generations. Annu. Rev. Neurosci. 24, 1161–1192.
Miguel, H.O., Lisboa, I.C., Gonçalves, Ó.F., Sampaio, A., 2019. Brain mechanisms for processing discriminative and affective touch in 7-month-old infants. Dev. Cogn. Neurosci. 35, 20–27. doi:10.1016/j.dcn.2017.10.008.
Morrison, I., 2016. ALE meta-analysis reveals dissociable networks for affective and discriminative aspects of touch. Hum. Brain Mapp. 37 (4), 1308–1320. doi:10.1002/hbm.23103.
Morrison, I., Björnsdotter, M., Olausson, H., 2011. Vicarious responses to Social Touch in Posterior Insular Cortex Are Tuned to Pleasant Caressing Speeds. J. Neurosci. 31, 9554–9562.
Mozumder, M., 2015. Image Reconstruction with Error Modelling in Diffuse Optical Tomography. University of Eastern Finland PhD thesis.
Mäkelä, T., Clarysse, P., Lötjönen, J., Sipilä, O., Lauerma, K., Hänninen, H., Pyökkimies, E.P., Nenonen, J., Knuuti, J., Katila, T., Magnin, I.E., 2001. A new method for the registration of cardiac PET and MR images using deformable model based segmentation of the main thorax structures. Med. Image Comput. Comput. - Assisted Intervent. – MICCAI 2001 Lect. Notes Comput. Sci. 557–564. doi:10.1007/3-540-45468-3_67.
Mörelius, E., Örtenstrand, A., Theodorsson, E., Frostell, A., 2015. A randomised trial of continuous skin-to-skin contact after preterm birth and the effects on salivary cortisol, parental stress, depression, and breastfeeding. Early Hum. Dev. 91 (1), 63–70. doi:10.1016/j.earlhumdev.2014.12.005.
Nissilä, I., Kotilahti, K., Fallström, K., Katila, T., 2002. Instrumentation for the accurate measurement of phase and amplitude in optical tomography. Rev. Sci. Instrum. 73 (9), 3306–3312. doi:10.1063/1.1497496.
Nissilä, I., 2004. Instrumentation for Medical Optical Tomography with Applications. Helsinki University of Technology D. *Sc*. Thesis http://urn.fi/urn:nbn:fi:tkk-004553.
Nissilä, I., Noponen, T., Kotilahti, K., Katila, T., 2005a. Instrumentation and calibration methods for the multichannel measurement of phase and amplitude in optical tomography. Rev. Sci. Instrum. 76, 044302. doi:10.1063/1.1884193.
Nissilä, I., Noponen, T., Heino, J., Kajava, T., Katila, T., 2005b. Diffuse optical imaging. In: Advances in Electromagnetic Fields in Living Systems book series (AEFL, volume 4), pp. 77–129.
Näsi, T., Mäki, H., Hiltunen, P., Heiskala, J., Nissilä, I., Kotilahti, K., Ilmoniemi, R.J., 2013. Effect of task-related extracerebral circulation on diffuse optical tomography: experimental data and simulations on the forehead. Biomed. Opt. Express 4, 412.
Nordin, M., 1990. Low-threshold mechanoreceptive and nociceptive units with unmyelinated I fibres in the human supraorbital nerve. J. Physiol. (Lond.) 426, 229–240.
Okada, E., Firbank, M., Schweiger, M., Arridge, S.R., Cope, M., Delpy, D.T., 1997. Theoretical and experimental investigation of near-infrared light propagation in a model of the adult head. Appl. Opt. 36 (1), 21–31.
Okada, E., Delpy, D.T., 2003. Near-infrared light propagation in an adult head model. I. Modeling of low-level scattering in the cerebrospinal fluid layer. Appl. Opt. 42, 2906–2914.
Olausson, H., Lamarre, Y., Backlund, H., Morin, C., Wallin, B.G., Starck, G., Ekholm, S., Strigo, I., Worsley, K., Vallbo, A.B., Bushnell, M.C., 2002. Unmyelinated tactile afferents signal touch and project to insular cortex. Nat. Neurosci. 5 (9), 900–904. doi:10.1038/nn896.
Olausson, H.W., Cole, J., Vallbo, A., McGlone, F., Elam, M., Krämer, H.H., Rylander, K., Wessberg, J., Brushnell, M.C., 2008. Unmyelinated tactile afferents have opposite effects on insular and somatosensory processing. Neurosci. Lett. 436, 128–132.
Olausson, H., Wessberg, J., Morrison, I., Mcglone, F., Vallbo, Å., 2010. The neurophysiology of unmyelinated tactile afferents. Neurosci. Biobehav. Rev. 34 (2), 185–191. doi:10.1016/j.neubiorev.2008.09.011.
Pawling, R., Cannon, P.R., McGlone, F.P., Walker, S.C., 2017. C-tactile afferent stimulating touch carries a positive affective value. PLoS ONE 12 (3), e0173457. doi:10.1371/journal.pone.0173457.
Perini, I., Olausson, H., Morrison, I., 2015. Seeking pleasant touch: neural correlates of behavioral preferences to skin stroking. Front. Behav. Neurosci. 9, 1–9 8.
Pinti, P., Aichelburg, C., Gilbert, S., Hamilton, A., Hirsch, J., Burgess, P., Tachtsidis, I., 2018. A review on the use of wearable functional near-infrared spectroscopy in naturalistic environments. Jpn. Psychol. Res. 60, 347–373.
Pirazzoli, L., Lloyd-Fox, S., Braukmann, R., Johnson, M., Gliga, T., 2019. Hand or spoon? Exploring the neural basis of affective touch in 5-month-old infants. Dev. Cogn. Neurosci. 35, 28–35. doi:10.1016/j.dcn.2018.06.002.
Rolls, E.T., 1999. The functions of the orbitofrontal cortex. Neurocase 5, 301–312. doi:10.1080/13554799908411984.
Rolls, E.T., Kringelbach, M.L., Odoherty, J., Francis, S., Bowtell, R., Mcglone, F., 2001. Pleasant and painful touch are represented in the human orbitofrontal cortex. Neuroimage 13 (6), 468. doi:10.1016/s1053-8119(01)91811-7.
Rolls, E.T., O' Doherty, J., Kringelbach, M.L., Francis, S., Bowtell, R., McGlone, F, 2003. Representations of pleasant and painful touch in the human orbitofrontal and cingulate cortices. Cereb. Cortex 13, 308–317.
Rolls, E.T., 2019. The cingulate cortex and limbic systems for emotion, action, and memory. Brain Struct. Funct. 224, 3001–3018.
Sailer, U., Triscoli, C., Häggblad, G., Hamilton, P., Olausson, H., Croy, I., 2016. Temporal dynamics of brain activation during 40 min of pleasant touch. Neuroimage 139, 360–367.
Salli, E., Korvenoja, A., Visa, A., Katila, T., Aronen, H.J., 2001. Reproducibility of fMRI: effect of use of contextual information. Neuroimage 13, 459–471.
Schmidt, F.E., 2000. Development of a time-resolved optical tomography system for neonatal brain imaging. Med. Phys. 27, 1343. doi:10.1118/1.599011, -1343.
Schweiger, M., Arridge, S.R., Nissilä, I., 2005. Gauss-Newton method for image reconstruction in diffuse optical tomography. Phys. Med. Biol. 50, 2365.
Schweiger, M., Dorn, O., Zacharopoulos, A., Nissilä, I., Arridge, S. R., 2010. 3D level set reconstruction of model and experimental data in Diffuse Optical Tomography. Opt. Express 18, 150–164. doi:10.1364/OE.18.000150.

Schweiger, M., Nissilä, I., Boas, D., Arridge, S, 2007. Image reconstruction in optical tomography in the presence of coupling errors. Appl. Opt. 46, 2743–2756.
Selb, J., Ogden, T.M., Dubb, J., Fang, Q., Boas, D.A., 2014. Comparison of a layered slab and an atlas head model for Monte Carlo fitting of time-domain near-infrared spectroscopy data of the adult head. J. Biomed. Opt. 19 (1), 016010.
Shi, F., Yap, P., Wu, G., Jia, H., Gilmore, J.H., Lin, W., Shen, D., 2011. Infant brain atlases from neonates to 1- and 2-Year-Olds. PLoS ONE 6 (4). doi:10.1371/journal.pone.0018746.
Shorey, S., He, H., Morelius, E., 2016. Skin-to-skin contact by fathers and the impact on infant and paternal outcomes: an integrative review. Midwifery 40, 207–217. doi:10.1016/j.midw.2016.07.007.
Simpson, C.R., Kohl, M., Essenpreis, M., Cope, M., 1998. Near-infrared optical properties of ex vivo human skin and subcutaneous tissues measured using the Monte Carlo inversion technique. Phys. Med. Biol. 43 (9), 2465.
Strangman, G., Franceschini, M.A., Boas, D.A., 2003. Factors affecting the accuracy of near-infrared spectroscopy concentration calculations for focal changes in oxygenation parameters. Neuroimage 18 (4), 865–879.
Tegenthoff, M., Ragert, P., Pleger, B., Schwenkreis, P., Förster, A., Nicolas, V., Dinse, H.R., 2005. Improvement of tactile discrimination performance and enlargement of cortical somatosensory maps after 5Hz rTMS. PLoS Biol. 3 (11). doi:10.1371/journal.pbio.0030362.
Torricelli, A., Pifferi, A., Taroni, P., Giambattistelli, E., Cubeddu, R., 2001. In vivo optical characterization of human tissues from 610 to 1010nm by time-resolved reflectance spectroscopy. Phys. Med. Biol. 46 (8), 2227.
Triscoli, C., Olausson, H., Sailer, U., Ignell, H., Croy, I., 2013. CT-optimized skin stroking delivered by hand or robot is comparable. Front. Behav. Neurosci. 7, 208. doi:10.3389/fnbeh.2013.00208.
Tuulari, J.J., Scheinin, M.N., Lehtola, S., Merisaari, H., Saunavaara, J., Parkkola, R., Sehlstedt, I., Karlsson, L., Karlsson, H., Björnsdotter, M., 2019. Neural correlates of gentle skin stroking in early infancy. Dev. Cogn. Neurosci. 35, 36–41. doi:10.1016/j.dcn.2017.10.004.
van der Zee, P., 1993a. Measurement and Modelling of the Optical Properties of Human Tissue in the Near Infrared. University College London Ph.D. thesis.
Van der Zee, P., Essenpreis, M., Delpy, D.T., 1993b. Optical properties of brain tissue. *Photon Migration and Imaging in Random Media and Tissues*. In: Proceeding of the SPIE 1888. International Society for Optics and Photonics, pp. 454–465.
Vallbo, Å., Olausson, H., Wessberg, J., Norrsell, U., 1993. A system of unmyelinated afferents for innocuous mechanoreception in the human skin. Brain Res. 628, 301–304. doi:10.1016/0006-8993(93)90968-S.
Vallbo, A.B., Olausson, H., Wessberg, J., 1999. Unmyelinated afferents constitute a second system coding tactile stimuli of the human hairy skin. J. Neurophysiol. 81, 2753–2763. doi:10.1152/jn.1999.81.6.2753.
Velandia, M., Uvnäs-Moberg, K., Nissen, E., 2012. Sex differences in newborn interaction with mother or father during skin-to-skin contact after Caesarean section. Acta Paediatr. 101 (4), 360–367. doi:10.1111/j.1651-2227.2011.02523.
Voos, A.C., Pelphrey, K.A., Kaiser, M.D., 2013. Autistic traits are associated with diminished neural response to affective touch. Soc. Cogn. Affect. Neurosci. 8, 378–386. doi:10.1093/scan/nss009.
Wu, X., Eggebrecht, A.T., Ferradal, S.L., Culver, J.P., Dehghani, H., 2014. Quantitative evaluation of atlas-based high-density diffuse optical tomography for imaging of the human visual cortex. Biomed. Opt. Express 5 (11), 3882–3900.
Wu, X., Eggebrecht, A.T., Ferradal, S.L., Culver, J.P., Dehghani, H., 2015. Evaluation of rigid registration methods for whole head imaging in diffuse optical tomography. Neurophotonics 2 (3), 035002.
Yao, R., Intes, X., Fang, Q., 2018. Direct approach to compute Jacobians for diffuse optical tomography using perturbation Monte Carlo-based photon "replay. Biomed. Opt. Express 9 (10), 4588–4603.
Yaroslavsky, A.N., Schulze, P.C., Yaroslavsky, I.V., Schober, R., Ulrich, F., Schwarzmaier, H.J., 2002. Optical properties of selected native and coagulated human brain tissues in vitro in the visible and near infrared spectral range. Phys. Med. Biol. 47 (12), 2059.
Yu, L., Nina-Paravecino, F., Kaeli, D., Fang, Q., 2018. Scalable and massively parallel Monte Carlo photon transport simulations for heterogeneous computing platforms. J. Biomed. Opt. 23 (1), 010504.
Zeff, B.W., White, B.R., Dehghani, H., Schlaggar, B.L., Culver, J.P., 2007. Retinotopic mapping of adult human visual cortex with high-density diffuse optical tomography. Proc. Natl. Acad. Sci. U.S.A. 104 (29), 12169–12174. doi:10.1073/pnas.0611266104.
Zhao, J., Ding, H.S., Hou, X., Zhou, C., Chance, B., 2005. In vivo determination of the optical properties of infant brain using frequency-domain near-infrared spectroscopy. J. Biomed. Opt. 10 (2), 024028.